Acta Materialia 278 (2024) 120230

Contents lists available at ScienceDirect

Acta Materialia

journal homepage: www.elsevier.com/locate/actamat

# Point defects in $BaSi_2$ identified and analyzed by electron paramagnetic resonance, photoluminescence and density functional theory

Takuma Sato [a,b,c], Jean-Marie Mouesca [b], Anne-Laure Barra [d], Didier Gourier [e], Motoharu Imai [f], Takashi Suemasu [a], Serge Gambarelli [b,*]

[a] Institute of Applied Physics, University of Tsukuba, Tsukuba, Ibaraki 305-8573, Japan
[b] University Grenoble Alpes, CEA, CNRS, IRIG, SyMMES, CAMPE, F-38000 Grenoble, France
[c] EPR Research Group, Max Planck Institute for Chemical Energy Conversion, Mülheim an der Ruhr 45470, Germany
[d] LNCMI-CNRS, EMFL, Université Grenoble-Alpes, Université Toulouse 3, INSA Toulouse, F-38000 Grenoble, France
[e] Chimie ParisTech, PSL University, CNRS, Institut de Recherche de Chimie de Paris, UMR8247, 11 rue Pierre et Marie Curie, 75005 Paris, France
[f] Research Center for Electrical and Optical Materials, National Institute for Materials Science, Ibaraki 305-0047, Japan

ARTICLE INFO

*Keywords:*
Electron paramagnetic resonance
Semiconductor compounds
Defects
Photoluminescence
Density Functional Theory

Barium disilicide ($BaSi_2$) is a semiconductor with promising photovoltaic properties. To build efficient devices, a good understanding of its defects is required. In this article, we present the first systematic study of such defects in a series of $BaSi_2$ samples synthetized in Barium-rich and Silicon-rich conditions. We combined electron paramagnetic resonance (EPR), Photoluminescence (PL) and density functional theory (DFT) to complete our analysis. With these techniques, we spectroscopically characterized five paramagnetic defect centers (defect 1 to defect 5) and four PL centers (P0 to P3). We identified several of them: in Ba-rich conditions, defect 5 corresponds to the negatively charged silicon vacancy $V_{Si}^{-1}$. In Si-rich conditions, defect 1 and defect 2 correspond to a negatively charged complex defect $O_{Si}^{-1}$, consisting of a pseudotetrahedron of 3 silicon and 1 oxygen in two slightly different environments. For PL, we attributed two bands (P0 and P1) to transitions involving $O_{Si}$ once again; P2 and P3 were attributed to transitions involving another complex defect $[O_iS_i]$, an interstitial silicon in close proximity to an interstitial oxygen. The existence of these defects rationalizes previous reports in the literature, in particular the increased photoresponse upon hydrogen passivation.

## 1. Introduction

Barium disilicide ($BaSi_2$) – composed of abundant, inexpensive, and eco-friendly elements – has been drawing attention as a useful platform in a wide variety of fundamental and applied scenarios. The properties of interest include its superconductivity, promising thermoelectric properties (relatively high Seebeck coefficient with outstanding low thermal conductivity), as well as optical properties compatible with photovoltaic (PV) devices.[1–8] Its multifunctional nature derives from a complex and distinctive crystal structure ($BaSi_2$-type, orthorhombic, space group: *Pnma* (No. 62), $Z = 8$) combining an alkaline-earth metal (Ba) with group 14 elements (Si).[9] The special structural motif has been explained in accordance with the Zintl-Klemm concept.[10] Thus, Ba atoms donate their valence electrons to Si atoms, and four Si atoms form covalent bonds so as to satisfy the octet (8-N) rule (Fig. 1).[11] The Ba-to-Si charge transfer was confirmed by $^{29}Si$ nuclear magnetic resonance spectroscopy applied to an orthorhombic $BaSi_2$.[12] The first principle calculations based on density functional theory (DFT) also confirmed the charge transfer and covalent-bond formation.[13–15]

We are particularly interested in potential applications of $BaSi_2$ in PV, based on its excellent properties: a suitable band gap in the 1.13–1.30-eV range, large absorption coefficient ($> 10^5$ $cm^{-1}$ for photon energies above 1.5 eV), long minority-carrier diffusion length (~10 μm) and lifetime (~10 μs) obtained on high-quality undoped $BaSi_2$ epitaxial films grown under stoichiometric conditions (with subsequent post-growth annealing or hydrogen treatments), as well as the possibility to control bipolar conductivity through impurity doping.[7,16–23] One of the most remarkable characteristics of $BaSi_2$ is its large light absorption coefficient (α) despite its indirect semiconductor properties. p-$BaSi_2$/n-Si heterojunction PV devices, where p-$BaSi_2$ acts as a hole transport layer, are reported to have an efficiency of up to 10.62 %, which is the highest conversion efficiency along silicide-based PV devices.[24] Recently, our team also demonstrated the operation of homojunction PV devices ($\eta = 0.48\%$).[25] Consequently, $BaSi_2$ may be

* Corresponding author.
*E-mail address:* serge.gambarelli@cea.fr (S. Gambarelli).

https://doi.org/10.1016/j.actamat.2024.120230
Received 13 December 2023; Received in revised form 25 July 2024; Accepted 28 July 2024
Available online 29 July 2024

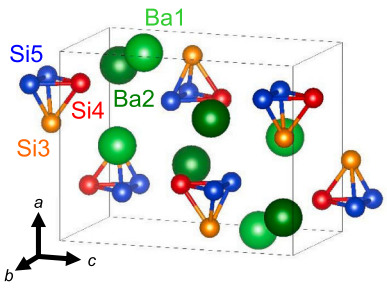


**Fig. 1.** Schematic crystal structure of orthorhombic $BaSi_2$. Two inequivalent barium atoms (Ba1 and Ba2) and three inequivalent silicon atoms (Si3, Si4, and Si5) are present in this cell (see also Figure S20).

a good candidate for the production of post-silicon or next-generation thin-film PV devices.

According to our device simulation, the conversion efficiency of thin-film PV devices with a $BaSi_2$ absorber layer could reach a maximum of 25 %, assuming zero reflectivity at the surface and a minority carrier diffusion length of 10 μm and lifetime of 10 μs.[26,27] This would be a considerable improvement compared to current device performances. Hara *et al.* systematically investigated minority carrier lifetime of undoped $BaSi_2$ epitaxial films.[20] They found that post-growth annealed films showed improvement in photoconductivity by two orders larger than as-grown films. They pointed out that $BaSi_2$ potentially possessed bulk minority carrier lifetime of ~10 μs. Independently, Xu *et al.* reported inferior minority carrier lifetime in as-grown undoped $BaSi_2$ film can be improved by supplying hydrogen onto as-grown film.[28] With this hydrogen treatment, a minority carrier lifetime improved up to ~10 μs. Both studies infer that as-grown undoped $BaSi_2$ films, which was adopted in the previous homojunction PV device,[25] may contain defects. Thus, one of the key factors in play in PV systems is "point defects", which often unintentionally deteriorate the performance of semiconductor-based devices. Deep defects within the bandgap in epitaxial $BaSi_2$ films have been explored by deep level transient spectroscopy (DLTS),[29,30] and positron annihilation spectroscopy was used to clarify the nature of vacancy-type defects present in the films.[31,32] Elsewhere, temperature-dependent resistivity and photoluminescence (PL) spectroscopy were used to investigate defect-induced levels within the bandgap.[16,17,21,33,34] Theoretical calculations indicate that the experimental results obtained are likely to derive from silicon vacancies.[35] This crucial defect requires sophisticated control if we are to design photovoltaic devices with higher performance. However, despite considerable effort, no complete picture has yet been presented for it – possibly because microscopic insights into such defects have yet to be directly accessed.

Electron paramagnetic resonance (EPR) is one of the most powerful spectroscopies to explore the microscopic structures of defects in semiconductors. For instance, in crystalline Si (c-Si), numerous paramagnetic defects have been described thanks to EPR.[36–40] Here, we made use of various advanced EPR techniques (multi-frequency, hyperfine sublevel correlation, electron-nuclear double resonance, and electron-electron double resonance detected NMR) as well as of the standard continuous wave EPR spectroscopy.[41–43] We combined these techniques with photoluminescence, the results of which are compared to theoretical calculations based on the density functional theory (DFT) to present the first systematic study of defects in $BaSi_2$.

## 2. Experimental methods

### 2.1. Sample preparation

Samples were prepared by Ar-arc melting. To systematically investigate defects in $BaSi_2$, 1:$x_s$ ($x_s$ = 1.88, 1.90, 1.94, 2.00, 2.06, and 2.10) molar mixtures of Ba (nominal purity 3 N) and c-Si (nominal purity 10 N) were prepared as starting materials. The starting materials were arc melted on a water-cooled copper hearth under an Ar atmosphere at a pressure of approximately 0.07 MPa. We typically repeat the melting and turning over three times for the reaction, and repeat it further three times for homogenization.

### 2.2. Sample characterization

The overall chemical compositions of samples were determined by inductively coupled plasma optical emission spectroscopy (ICP-OES). Data were collected using the ICP-OES instrument (Agilent, 720ES).

Powder X-ray diffractometry (XRD) was used to analyze the phases in samples. XRD patterns were measured using a Bragg-Brentano diffractometer with the D/teX detector (Rigaku, RINT-TTR-III). CuKα radiation (40 kV, 150 mA), and a step size of 0.02° were applied in the 2$\theta$ range of 5.00°–100.00° at room temperature, 297 K.

Electron-probe microanalysis (EPMA) was also undertaken with a JEOL JXA-8900 operated at an acceleration voltage of 15 kV and a beam current of 50 nA. $BaAl_4$, and c-Si were used as standard materials. For these analyses, samples were mounted in resin and polished using an oil-based diamond slurry.

Full details of sample preparation and characterization can be found elsewhere.[44]

### 2.3. EPR

X-band continuous wave EPR (CW-EPR) experiments were performed on an EMX Bruker spectrometer with an ER-4116 dual mode cavity and an ESR-900 Helium flow cryostat. Q-band CW-EPR, Q-band pulsed EPR and pulsed X-band EPR experiments were performed on an Elexsys E-580 Bruker spectrometer with a Bruker EN5107D2 Q-band cavity or a Bruker ER4118X-MS5 X-band cavity. The cavity was cooled by a continuous helium flow cryostat (Oxford CF935).

High-frequency EPR spectra were recorded on a multi-frequency spectrometer operating in a double-pass configuration. A 127-GHz frequency source (Virginia Diodes Inc.) combined with a voltage doubler or tripler was used. The excitation light source was propagated through a Quasi-Optical bridge (Thomas Keating) outside the cryostat, and through a corrugated waveguide inside it. Signal was detected with a hot electron InSb bolometer (QMC Instruments). Measurements were made at 25 K, using a field modulation of ~1.7 mT and a 1 mT $s^{-1}$ field-sweep rate. The main magnetic field was supplied by a 16 T superconducting magnet associated with a variable temperature insert (Cryogenic).

Electron-spin-echo (ESE) spectra were produced using the standard Hahn-echo sequence: $\pi/2$-$\tau$-$\pi$-$\tau$-echo, with microwave (mw) pulse lengths $t_{\pi/2}$ = 16 ns, $t_\pi$ = 32 ns, and $\tau$ = 200 ns. Spin-lattice relaxation time ($T_1$) was measured by the inversion recovery method: $\pi$-$T$-$\pi/2$-$\tau$-$\pi$-$\tau$-echo, using the same mw pulse lengths and incrementing $T$ in 5 μs (or 0.5 μs) steps. Spin-spin relaxation time ($T_2$) experiments were based on the following pulse sequence: $\pi/2$-$\tau$-$\pi$-$\tau$-echo, with mw pulse lengths $t_{\pi/2}$ = 16 ns and $t_\pi$ = 32 ns; $\tau$ was incremented stepwise, in 30 ns (for X-band) and 100 ns (for Q-band) steps. HYSCORE spectra were recorded at 10 K using the standard 4-pulse sequence ($\pi/2$-$\tau$-$\pi/2$-$t_1$-$\pi$-$t_2$-$\pi/2$-$\tau$-echo) with $t_{\pi/2}$ = 16 ns, $t_\pi$ = 32 ns, and $\tau$ = 140 ns. Unwanted echoes were removed by four-step phase cycling. A 128×128 data set was recorded with times $t_1$ and $t_2$, incremented in 24 ns steps from an initial value of 200 ns. This data set was processed using XEPR software (Bruker). The two-dimensional Fourier transform magnitude spectrum was calculated and is presented as a contour plot. ENDOR spectra were recorded at 8 K using the Davies-type pulse sequence: $t_{inv}$-$t_{RF}$-$T$-$\pi/2$-$\tau$-$\pi/2$-$\tau$-echo with a 32 ns non-selective inversion pulse length ($t_{inv}$), a 20 μs long radio frequency (RF) pulse ($t_{RF}$), a delay time $T$ = 4 μs, mw pulse lengths of $t_{\pi/2}$ = 16 ns and $t_\pi$ = 32 ns, and $\tau$ = 200 ns. To suppress artefacts due to long nuclear relaxation times, a RF sweep was performed in stochastic mode (range 1–195 MHz with a frequency increment of 0.1 MHz). Electron-electron double resonance detected nuclear magnetic resonance (ED-

NMR) experiments were performed at Q-band. Spectra were recorded at 8 K using the following pulse sequence: $t_{HTA}$-$T$-π/2-$\tau$-π/2-$\tau$-echo with $t_{HTA} = 10$ μs, $T = 10$ μs, $t_{\pi/2} = 400$ ns, $t_{\pi} = 800$ ns, and $\tau = 2500$ ns. A high-turning angle (HTA) pulse with a Gaussian shape was applied using a Bruker SpinJet-AWG to somewhat reduce the problem of the central blind spot mentioned by Prisner.[45] The sweep width of the frequency of the HTA pulse was 512 MHz, with a frequency increment of 1 MHz.

Spin concentration was measured in X-band CW-EPR by comparison with samples of TEMPO solutions with known concentrations in ortho-terphenyl glass.

EPR spectra were simulated using the "pepper" routine available in the Easyspin package.[46]

### 2.4. Photoluminescence

Temperature-dependent photoluminescence (PL) was measured with polycrystalline samples over the temperature range 8–70 K. A continuous wave 442-nm He-Cd laser with a constant power of 60 mW/cm$^2$ was used as the excitation source for PL measurement. Luminosity, analyzed by a single monochromator (Ritu Oyo Kogaku Co., Ltd. MC-25 N) with a focal length of 25 cm, was detected by a liquid nitrogen cooled InP/InGaAs photomultiplier (Hamamatsu Photonics R5509–72) and amplified by a lock-in technique (NF Corp. LI5640).

### 2.5. Computational methods

DFT calculations were performed using the QUANTUM ESPRESSO (QE 6.4) code to help identify the defects observed in both Si-rich and Ba-rich conditions.[47] The geometry of all diamagnetic and paramagnetic defects was optimized using the pw.x subroutine. DOS plots, band structures, and contents were extracted using subroutines dos.x and projwfc.x.

The Perdew−Burke−Ernzerhof version of the generalized gradient approximation of the exchange-correlation functional (GGA-PBE) was used throughout.[48] Si and Ba pseudopotentials prepared by A. Dal Corso (Si.pbe-mt_gipaw.UPF, Ba.pbe-tm-gipaw-dc.UPF) were used for intrinsic defects. In addition (see details in the DFT results section below) oxygen-related defects (passivated or not by hydrogen atoms) were also considered, and oxygen and hydrogen pseudopotentials were used (O.pbe-tm-gipaw.UPF and H.pbe-tm-gipaw.UPF).

Though not the primary focus of the investigation, diamagnetic (neutral and charged) defects were also considered. Kumar et al. explored the phase diagram for the Ba-Si system as well as the formation energies for both neutral and charged intrinsic defects.[35] We therefore first attempted to obtain the same results and trends for i) the phase diagram for the BaSi system (Ba, $Ba_2Si$, $Ba_5Si_3$, BaSi, $Ba_3Si_4$, $BaSi_2$, Si) and corresponding Si and Ba chemical potentials (see Supplementary Material for further details: Figs. S21-S23; Tables S3–4), ii) formation enthalpies for each phase (Figure S24; Table S5), iii) the band structure of the bulk material (Figure S25), iv) intrinsic formation energies for $BaSi_2$ (neutral and charged) (Figs. S26-S27; Tables S6–11). We considered some oxygen-related defects, for which we also computed formation energies (Figs. S28-S31; Tables S12–13), as well as the effect of passivation by hydrogen atoms (Figs. S32–34). For paramagnetic defects, the QE subroutine gipaw.x (GIPAW for Gauge-Including Projector-Augmented Wave) was used to compute g tensors, hyperfine coupling tensors ($^{29}$Si, $^{135/137}$Ba), and quadrupole tensors ($^{135/137}$Ba).[49] The kinetic energy cut-off for wavefunctions was set to 30 Ry, for charge density and potential it was set to 240 Ry. The "K_POINTS automatic" feature is suitable for gipaw.x calculations and was used throughout.

DFT calculations were performed in two steps. First, because of the large number of defects and charge states, all the above-mentioned defect models for 2 × 2 × 1 super-cells were explored (i.e., 96 atoms for the bulk model, within a box of size 2a = 17.84 Å, 2b = 13.60 Å, $c$ = 11.58 Å), with a crude $k$-point mesh of 1 × 1 × 1. Second, likely candidates for intrinsic defects and oxygen-based defects of interest were selected. The g tensor and hyperfine calculations were repeated on this selection with a finer 2 × 2 × 2 $k$-point mesh. Finally, to test result accuracy, $V_{Si}^{-1}$ was singled out to compare hyperfine coupling constants for 1 × 1 × 1, 2 × 2 × 1 and 2 × 2 × 2 super-cells (see SI: Table S18) combined with both $k$-point meshes – 1 × 1 × 1 and 2 × 2 × 2 (SI). These tests confirmed hyperfine coupling constants (hcc) to be good probes of the extent and stability of the computed spin densities. The g tensor values were also determined in the same conditions (except for the final 2 × 2 × 2 super-cell and $k$-point mesh in the 2 × 2 × 2 combination, as this condition failed to converge despite the use of a dedicated 128-core node: Table S19).

## 3. Results

### 3.1. Structural and optical characterization

To systematically investigate defects in $BaSi_2$, we prepared a series of six starting material samples with different Si-to-Ba ratios, $x_s$ (Table 1). The ideal stoichiometry is equal to 2. After synthesis, we determined the atomic Si-to-Ba ratio in bulk samples by ICP-OES (designated as $x_{ICP\text{-}OES}$), and local atomic ratios by EPMA (designated as $x_{EPMA}$). The Cu concentration is under the detection limit (0.001 wt.%). We observed that the $x_{ICP\text{-}OES}$ ratio measured was slightly higher than the starting ratio $x_s$, indicating evaporation of Ba during the arc melting process. We ranked samples based on the $x_{ICP\text{-}OES}$ values measured. Four samples (A, B, C, and D) were found to be "Si-rich" with stoichiometries ranging from $x_{icp\text{-}OES} = 2.40$ to 2.05. The last two samples (E and F) were "Ba-rich" with $x_{ICP\text{-}OES} = 1.94$ and 1.88 (Table 1).

The upper left panel of Figs. 2a and 2b shows the back-scattered electron (BSE) images of Si-rich ($x_{ICP\text{-}OES} = 2.40$) and Ba-rich ($x_{ICP\text{-}OES} = 1.92$) samples. EPMA results at position of grains show $x_{EPMA} = 2.00$ for both samples, as listed in Table 1, indicating that the main phase of samples is $BaSi_2$. The upper right panels are expanded BSE image and Ba, Si, and O images of inter-domain area, surrounded by the dashed square of the upper left panel. In the Si-rich samples, c-Si (black area) appears as the second phase. In the Ba-rich samples, $Ba_3Si_4$ (white area) and its oxide (black area) appear at the inter-domain.

The lower panels of Figs. 2a and b demonstrate powder XRD patterns of Si-rich and Ba-rich samples (See Figure S1 for the full-range powder XRD pattern). Main peaks are attributed to the diffraction peaks from orthorhombic $BaSi_2$ (space group *Pnma* (No. 62) with lattice parameters of $a$ = 8.9326 Å, $b$ = 6.7262 Å, $c$ = 11.5335 Å).[34,50,51] The diffraction peaks from c-Si were observed at $2\theta = 47.5$ and 56.0 deg (Fig. 2a) in the Si-rich sample while that from $Ba_3Si_4$ was at $2\theta = 48.0$ deg in the Ba-rich sample (Fig. 2b). The XRD results support the presence of the second phases at the inter-domain as detected by the EPMA. The existence of Ba/Si ratio-dependent second phase is consistent with the

**Table 1**
Atomic ratios for investigated samples A-F. $x_s$ is the ratio of Ba to c-Si in the starting materials (also see, Section 2.1). $x_{ICP\text{-}OES}$ is the atomic ratio of the synthesized materials measured by ICP-OES, inferring some Ba evaporation during synthesis. $x_{EPMA}$ is the atomic ratio of $BaSi_2$ domains in the synthesized materials measured by EPMA. The numbers in parentheses are standard deviations. The values of $x_{EPMA}$ indicate that the $BaSi_2$ grains are almost stoichiometric (~2.00) within a standard deviation. The disagreements between $x_{ICP\text{-}OES}$ and $x_A$ appear to be due to precipitations of c-Si and $Ba_3Si_4$, as discussed in detail in the main text.

| Label | $x_s$ | $x_{ICP\text{-}OES}$ | $x_{EPMA}$ |
|---|---|---|---|
| A | 2.10 | 2.40 | 2.00(1) |
| B | 1.90 | 2.09 | 1.98(2) |
| C | 2.06 | 2.13 | 2.01(1) |
| D | 2.00 | 2.05 | 2.01(1) |
| E | 1.94 | 1.99 | 2.01(1) |
| F | 1.88 | 1.92 | 2.01(1) |

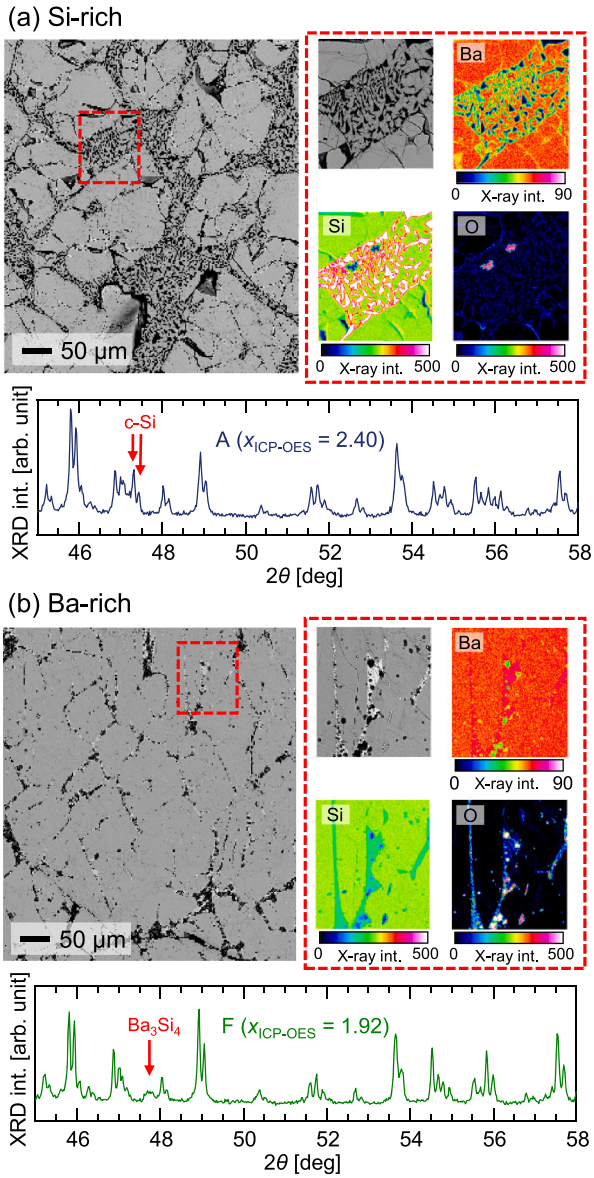


**Fig. 2.** Powder XRD patterns, back-scattered electron (BSE) images, and Ba, Si, O images of (a) Si-rich ($x$ = 2.40) and (b) Ba-rich ($x$ = 1.92) samples. Images in the dashed square are expanded views of the area in the dashed square of the BSE image on the left. The color bars below the mapping images indicate the characteristic X-ray intensity of each element.

phase diagram for the Ba-Si binary system.[52]

### 3.2. Paramagnetic defects

All samples were EPR-active below 50 K and exhibited complex spectra at all investigated frequencies (Fig. 3 and Figure S2-S3). At X-band, the spectra for samples A-D were mainly centered on $g$ = 2.003–2.005 (slightly above $g_e$ = 2.0023). In contrast, the spectra for samples E and F had completely different structures with extensions down to $g$ values of 1.84. (below $g_e$). However, the dichotomy was not strict, as small amounts of the predominant center in the Ba-rich samples was also observed in the Si-rich samples (arrows in Fig. 3a). This mixing of spectra was confirmed by the ESE-detected field-sweep spectra (Figure S4). Conversely, the high-field multi-frequency EPR measurements revealed the presence of Mn(II) ion impurities in the samples, partly masking the signals expected for defects 1 and 2 (see below). Nevertheless, the detectable signals are in line with what is expected

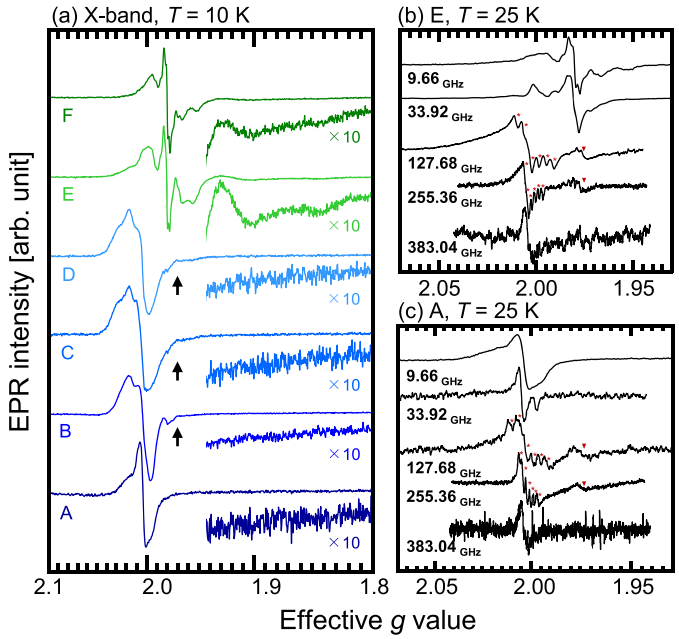


**Fig. 3.** (a) Normalized continuous wave EPR spectra of samples A-F recorded in X-band (9.7 GHz) at 10 K. Zero-crossing $g$ values are roughly estimated to be larger than 2 for Si-rich samples and less than 2 for Ba-rich samples, indicating that different family of paramagnetic centres are predominant. In Si-rich samples, the predominant centres in Ba-rich samples are also observed as minor centres and denoted by arrows. In samples E and F (Ba-rich), a relatively larger anisotropic centre is also found. Multi-frequency EPR spectra of (b) sample E (Ba-rich) and (c) sample A (Si-rich) infer that the predominant centre in Si-rich samples is also contained even under Ba-rich conditions. Stars(*) and triangle (▾) in (b) and (c) are considered to be $Mn^{2+}$ contained unintentionally and a paramagnetic centre from the sample tube, respectively.

from the analysis of X-band and Q-band results. They confirmed that the characteristic center from Si-rich samples was also present in Ba-rich samples (Figs. 3b and c). Numerous preliminary experiments (not shown here) demonstrated that these two spectral classes are consistently observed on $BaSi_2$ samples. The proportions of each signal depend on the Ba:Si stoichiometry. Taken together, these observations suggest that two distinct families of paramagnetic centers predominate in $BaSi_2$ generated under Si-rich or Ba-rich conditions. These changes occur smoothly (hence the minority species) at stoichiometry, but become detectable in Si-rich or Ba-rich conditions.

#### 3.2.1. Analysis of EPR spectra: number of different types of defects

All the features of spectra recorded for Si-rich samples (A-D) were the result of $g$ anisotropy, since in $g$ scale, spectra recorded at different frequencies were similar (except for linewidth, see Fig. 3c and Figure S3). In contrast, some frequency-independent structures were observed with the Ba-rich samples E and F (Fig. 3b). These structures indicate a contribution from either hyperfine coupling or zero field splitting.

The EPR spectra for samples A-D cannot be explained by a single paramagnetic species with a rhombic $g$ tensor. To disentangle these centers, a series of experiments was performed over a range of temperatures and microwave powers in CW X- and Q-bands (see Figure S5). The shape changes observed in these experiments indicated that at least two paramagnetic centers with different relaxation times were present in the spectrum for each sample. To further analyze the spectra, we performed pulsed EPR measurements and measured both the longitudinal relaxation time ($T_1$) and the transverse relaxation time ($T_2$*). Once again, two distinct centers were present in the Si-rich samples (see Figure S6).

To validate the existence of these two centers, for each composition

(A, B, C, and D) we simulated the CW X- and Q-band spectra for two species with rhombic $g$ tensors (Fig. 4 and Figs. S7-S8). All the patterns observed experimentally were accurately simulated. The tensors obtained were almost identical across all four compositions for the two distinct species simulated (Table 2). Hereafter, we refer to these species as defect 1 and defect 2 – with respective $g$ tensor values ($g_1$ =2.025, $g_2$ = 2.012, $g_3$ = 1.998) and ($g_1$ = 2.010, $g_2$ = 2.005, $g_3$ = 1.997). Fig. 4 shows the experimental EPR spectra alongside the simulated spectra. These four spectra can therefore be assumed to result from mixtures of defect 1 and defect 2 in various proportions. The linewidths measured for the four samples differed, and could be modeled by a mixture of $g$ tensor strain and unresolved hyperfine coupling and/or other transition-independent effects. Consequently, the linewidth variations are probably due to these basic effects combined with the samples' intrinsic crystallization qualities.

In Ba-rich samples, three distinct paramagnetic centers were observed (defect 3, defect 4, and defect 5) (see Fig. 4(c), sample E). Defect 3 had a very anisotropic $g$ tensor and became prominent below 25 K or in conditions where strong microwave power was applied (Figure S9). Two principal values of the $g$ tensor could be directly measured on the spectra ($g_1$ = 1.844, $g_2$ = 1.918). However, the third value was masked by lines corresponding to the other centers. The last value ($g_3$ = 2.001) was therefore determined using pulsed EPR, and by analyzing ESE spectra acquired with different parameters (see Figs. S10-S11 for further explanation).

The intensity of defect 4 decreased drastically above 50 K, and was very difficult to saturate (see Figure S12). Its detailed shape was very difficult to determine because none of the experimental conditions we tested led it to predominate. In addition, it was undetectable in pulsed EPR experiments, probably due to an excessively short relaxation time even at liquid helium temperatures (4.2 K). We therefore conservatively simulated this defect with a single Gaussian line centered around $g \sim 1.980$, which could be attributed to a species with an $S > 1/2$ system. [53,54] If this were the case, some EPR transitions should be observed at effective $g \neq 2$. However, no such line was detected, and consequently the true nature of this defect remains to be determined.

As mentioned above, defect 5 had characteristic features that are independent of microwave frequencies. When examining the X-band spectrum at 50 K, features positioned at ±60, ±120, and ±230 MHz relative to the narrow EPR line ($g \sim 1.982$) were clearly observed. $^{29}$Si, $^{135}$Ba, and $^{137}$Ba have nuclear spins of 1/2, 3/2, and 3/2 and natural abundances of 4.68 %, 6.59 %, and 11.23 %, respectively. It can therefore be inferred that the complex EPR spectrum is derived from hyperfine interactions with Ba and/or Si nuclei. In this case, the narrow central EPR line can be presumed to correspond to the case where the unpaired electron exists near the nucleus with $I = 0$. We successfully simulated experimental results for this defect (Fig. 4), and the hyperfine parameters are summarized in Table 2.

### 3.2.2. *Hyperfine spectroscopy*

The hyperfine parameters can be used to gain a greater understanding of the microscopic structure of paramagnetic defects. However, in our samples (except for defect 5), they were unresolved in both CW-EPR- and ESE-detected field-sweep spectra. Therefore, we used alternative pulse sequences, including HYSCORE, Davies ENDOR (Fig. 5a), and ED-NMR (Fig. 5b) to obtain hyperfine spectra.[41–43]

In Si-rich samples, HYSCORE spectra exhibited peaks corresponding to $^{29}$Si hyperfine coupling constants of 2–3 MHz (see Figs. S13-S14). This frequency seems too low to derive from an atom directly positioned on the defect. Nevertheless, low values are to be expected as HYSCORE is specialized in the detection of weak hyperfine couplings.[55] We therefore performed Q-band Davies ENDOR, which is compatible with the detection of stronger hyperfine couplings.[56] Fig. 5(c) shows the ENDOR spectrum recorded at 1203 mT for sample D. Despite an accumulation time of more than 12 h, the signal-to-noise ratio (S/N ratio) was very low, with only the NMR transitions corresponding to weakly-coupled $^{135}$Ba ($|\gamma|/2\pi$ = 4.258 MHz/T),$^{137}$Ba ($|\gamma|/2\pi$ = 4.763 MHz/T) and $^{29}$Si ($|\gamma|/2\pi$ = 8.465 MHz/T) visible. We therefore applied ED-NMR to improve the S/N ratio. Fig. 5(d) shows a clear peak at ±40 MHz. Taking into account the Larmor frequencies of the nuclei in this system (Ba and Si) under Q-band conditions, this spectrum should be interpreted in the strong coupling regime ($|A| > 2\nu_I$). The result

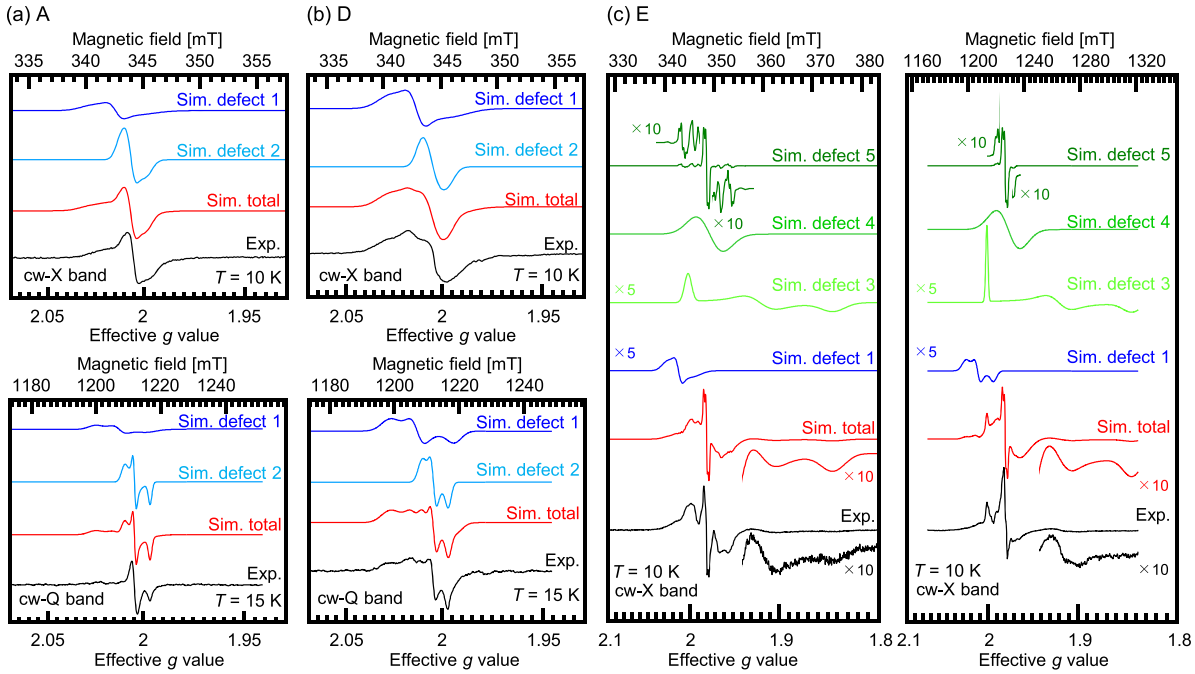


**Fig. 4.** Best simulated and experimental spectra for samples A (a), D (b), and E (c) at X- and Q-band. The overall spectral simulation (red curves) reproduces successfully experimental data (black). a) and b) The light blue and navy blue curves show spectral contributions of defect 1 and 2, respectively. (c) The blue, light green, green, and dark green curves show spectral contributions of defect 1, 3, 4, and 5, respectively. For all defects, the same parameters for EPR simulation (g tensor, hyperfine coupling) were used for X- and Q-band.

**Table 2**
Experimental and computed EPR parameters of species studied in this work. We can detect hyperfine coupling with CW EPR on defect5 only. It is necessary to use ENDOR or ED-NMR to obtain a rough evaluation of hyperfine coupling on defect1, defect 2, and defect 5. The very short relaxation time and broad linewidth precluded any hyperfine coupling evaluation for defect 3 and defect 4. Defect 1 and defect 2 cannot by safely disentangled at X-band and we assume that they have the same hyperfine coupling values. For computations, we used for $^{29}$Si : $g_n = -1.11058$, and for $^{137}$Ba : $g_n = +0.62491$. For each species and each atom type, only tensors with the biggest components are reported. $A_{av}$: average (isotropic) hyperfine value. $A_{an}$: anisotropic hyperfine value defined as the difference between maximal and minimal eigenvalues of the hyperfine tensor. Last column (Comment): Si3, Si4 and Si5 refer to silicon sites of Fig. 1. A and C refer to interstitial sites as defined by Imai and al.[48] The notations in parentheses (8c, 4b, 4c) correspond to positions (multiplicity and Wyckoff letter) of the orthorhombic, space group no. 62.

| Species | $g_1$ | $g_2$ | $g_3$ | $g_{av}$ | $\Delta g$ | $\lvert A_{av}(Si)\rvert$ (MHz) | $\lvert A_{an}(Si)\rvert$ (MHz) | $\lvert A_{av}(Ba)\rvert$(MHz) | $\lvert A_{an}(Ba)\rvert$ (MHz) | Comments |
|---|---|---|---|---|---|---|---|---|---|---|
| Defect 1 | 1.998 | 2.012 | 2.025 | 2.012 | 0.027 | 80 (EDNMR) | | | | Si rich |
| Defect 2 | 1.997 | 2.005 | 2.010 | 2.004 | 0.013 | 80 (EDNMR) | | | | Si rich |
| Defect 3 | 1.844 | 1.918 | 2.001 | 1.92 | 0.157 | Not detected | | | | Ba rich |
| Defect 4 | 1.98 | 1.98 | 1.98 | 1.98 | 0 | Not detected | | | | Ba rich, $S > 1/2$? |
| Defect 5 | 1.982 | 1.982 | 1.982 | 1.982 | 0 | 60, 120 (from CW EPR) 80 (from ENDOR) | | | | Ba rich |
| $V_{Si}^{-1}$ | 1.999 | 2.003 | 2.006 | 2.003 | 0.007 | 23.0,<br>22.1 | 83.5, 80.0 | 128.7, 123.2, 81.2, 79.4 | 14.0, 13.5, 10.8, 10.4 | Si3 (4c), Si5 (8c) |
| $V_{Si}^{+1}$ | 1.995 | 2.000 | 2.024 | 2.006 | 0.029 | 30.1, 19.8 | 135.2, 3.4 | 229.0<br>(36×2) | 25.0<br>(3 × 2) | Si3 (4c) |
| $Si_i^{-1}$ | 1.987 | 1.999 | 2.034 | 2.006 | 0.047 | 192.7, 142.3 | 22.8, 19.2 | 108.4 | 6.3 | C (4c) |
| $Si_i^{+1}$ | 1.999 | 2.033 | 2.065 | 2.032 | 0.066 | 20.2 × 2 | 4.4 | 15.4 | 3.2 | C (4c) |
| $Ba_{Si}^{+1}$ | 2.004 | 2.018 | 2.039 | 2.020 | 0.035 | 24.3, 24.1 | 85.8, 85.2 | 98.0, 97.4, 54.4, 50.1, 50.0 | 13.0, 12.9, 29.8, 10.3, 10.2 | Si3 (4c) |
| $Ba_{Si}^{+3}$ | 1.968 | 2.002 | 2.029 | 1.999 | 0.061 | 25.2 | 124.2 | 142.0<br>57.1<br>49.1 | 18.8<br>4.2<br>4.7 | Si3 (4c) |
| $O_{Si}^{+1}$ | 1.998 | 2.004 | 2.015 | 2.006 | 0.017 | 195.0 | 100.1 | 30.3<br>25.9 | 5.3<br>2.8 | Si5 (8c) |
| $O_{Si}^{-1}$ | 1.981 | 2.012 | 2.015 | 2.003 | 0.034 | 25.3, 23.6 | 78.8, 71.5 | 178,<br>132 | 16.0, 11.8 | Si5 (8c) |
| $O_{Si}^{-1}$ | 1.988 | 1.998 | 2.016 | 2.001 | 0.028 | 29.9 × 2 | 75.8 × 2 | 110.6 × 2<br>51.7 × 2 | 12.4 × 2<br>5.8 × 2 | Si4 (4c)<br>0.2 eV above Si5 (8c) |
| $O_i^{+1}$ | 1.989 | 2.362 | 2.422 | 2.257 | 0.433 | 10.5 | 6.6 | 47.2 | 3.5 | A (4b) |
| $O_i^{-1}$ | 1.978 | 1.984 | 2.005 | 1.989 | 0.027 | 264.8<br>22.1 | 30.4<br>91.4 | 290.5<br>69.4 | 21.2<br>4.8 | A (4b) |
| $[O_iSi_i]^{+1}$ | 1.996 | 2.027 | 2.045 | 2.023 | 0.049 | 250.6, 149.0 | 29.5,<br>5.3 | 125.4, 64.1 | 15.3, 11.4 | [A, A] (4b) |
| $[O_iSi_i]^{-1}$ | 1.601 | 1.951 | 2.089 | 1.880 | 0.488 | $< 5$ | $<12$ | 57.3<br>59.0 | 2.0<br>8.5 | [A, A] (4b) |

indicates that these species contain at least one hyperfine coupling of approximately 80 MHz. However, due to the overlap between the spectra for defect 1 and defect 2, we were unable to attribute these hyperfine couplings to one of these species. In addition, the ability of the ED-NMR sequence to detect hyperfine coupling is strongly dependent on the power and the length of the HTA pulse. We therefore cannot exclude that bigger or smaller hyperfine couplings may be present in these species but were not observable in our experimental conditions.

Applying the same strategy to Ba-rich samples, we performed several hyperfine spectroscopy measurements. Due to short relaxation time, only defect 5 could be studied. HYSCORE spectra exhibited a $^{29}$Si hyperfine coupling constant of 2–3 MHz once again, which is too small to explain the hyperfine splitting observed in the CW spectra. After an accumulation time of more than 12 h, Davies ENDOR spectra exhibited a very broad line, with a maximum at $|A/2| \sim 40$ MHz (Fig. 5e). Once again, this corresponds to a strong coupling regime, and the species present consequently contain at least one hyperfine coupling of approximately 80 MHz. ED-NMR analysis (Fig. 5f) produced peaks at 30–40 MHz almost matching those observed in the ENDOR spectrum. However, compared to the ENDOR spectrum, the S/N ratio was significantly improved, even with a relatively short accumulation time of 1–2 hours. Some additional features were observed at ±80–100 MHz and ±150–165 MHz, separated from one another by around 60 MHz. Due to the general difficulty of analyzing ED-NMR spectra at lower frequencies/fields, and the possible added complexity due to the finite bandwidth of the cavity used, we did not attempt to use these values to discriminate between our models.

In these experiments, we were unable to attribute the ENDOR or ED-NMR signals to Si or Ba hyperfine parameters due to a combination of modest signal/noise ratio, broad lines and inherent sequence limitation. However, it should be remembered that, all other things being equal, due to the difference in natural abundances, the hyperfine signal from Ba must be 3.8 times higher than the Silicon signal (6.59 + 11.2 % versus 4.67 %). In the absence of any extra broadening of the Ba signal due to quadrupolar coupling, these hyperfine parameters can therefore probably be attributed to Ba atoms.

#### 3.2.3. Spin concentration

We evaluated the spin concentrations of the five paramagnetic defects by comparing them to the integrated intensity of EPR spectra obtained for TEMPO at different known concentrations (Fig. 6, Figs. S15-S16, and Tables S1–2). It must be noted that the hypothesis used (i.e., that our samples only contained $S = 1/2$ species) can lead to substantial error, especially in Ba-rich conditions for defect 4. One last unknown parameter is the volume factor of the powder, i.e., the empty space between the grains of material in the sample holder. By visual inspection, we estimated this value to be approximately 0.5. The total concentrations and relative ratios within each family of defects (1, 2, vs 3, 4, 5) were roughly constant in Si-rich or Ba-rich conditions but changed rapidly between the two. We were unable to distinguish between defect 1 and defect 2 in Ba-rich conditions (sample E and F). The values obtained correspond to total paramagnetic defect concentrations varying from $7.3 \times 10^{16}$ cm$^{-3}$ (sample A) up to $3.8 \times 10^{18}$ cm$^{-3}$ (sample E).

### 3.3. Optically active defects

EPR is an ideal method for investigating the microscopic structures of paramagnetic defects. However, since not all defects are paramagnetic, we also used photoluminescence (PL) spectroscopy to analyze our samples. This highly sensitive method detects optically active defects. Fig. 7(a) shows PL spectra for samples A-F. The PL signal peaked at approximately 0.84 (P1), 1.04 (P2), and 1.15 (P3) eV, with relative

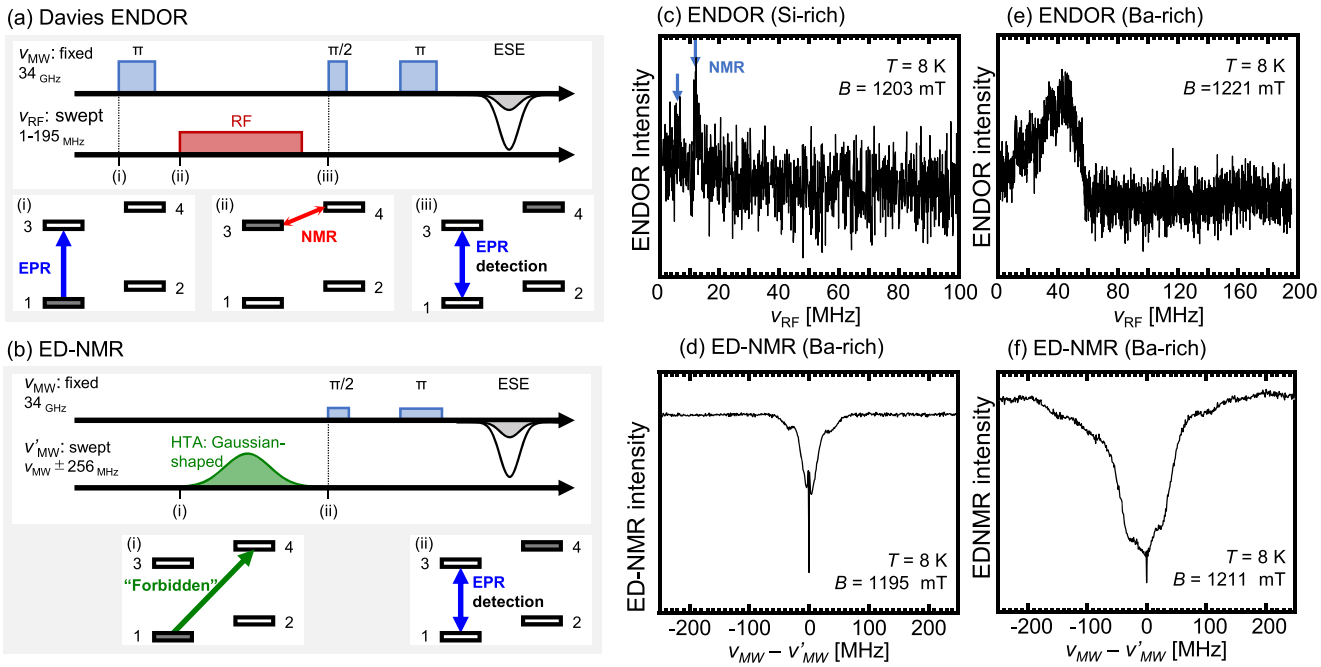


**Fig. 5.** Pulse sequences of (a) the Davies-type ENDOR and (b) the ED-NMR and their energy level diagram of $S = 1/2$, $I = 1/2$ during each sequence, where 1: $|\downarrow, \alpha>$, 2: $|\downarrow, \beta>$, 3: $|\uparrow, \alpha>$, and 4: $|\uparrow, \beta>$ by using the notation of $|S_z, I_z>$ (the electron spin magnetic quantum number, $S_z = \downarrow$ or $\uparrow$, and that of the nucleus, $I_z = \alpha$ or $\beta$). In the case of ENDOR, an inversion pulse is applied (1→3) at a time of (i), and then polarization can be transferred (3→4) when an applied radio-frequency ($\nu_{RF}$) matches NMR transitions. One can detect that change of the population via electron-spin-echo (ESE) intensity with the standard Hahn-echo sequence. In the ED-NMR sequence, an initial population transferred via the "forbidden" transition (1→4) with a relatively strong and long high-turning-angle (HTA) pulse (in this study, we applied the Gaussian-shaped HTA pulse instead of a usual rectangular-shaped one). ENDOR spectra of (c) sample D and (e) sample F are measured with a low signal to noise (S/N) ratio even after an accumulation time of more than 12 h. Peaks in (c) correspond to NMR transitions of $^{135}$Ba ($|\gamma|/2\pi = 4.258$ MHz/T) or $^{137}$Ba ($|\gamma|/2\pi = 4.763$ MHz/T) and $^{29}$Si ($|\gamma|/2\pi = 8.465$ MHz/T), whereas no clear spectrum considered as hyperfine couplings was confirmed in Si-rich samples. In contrast, a broad spectrum with its maximum at around 45 MHz seen in (e) corresponds to strong ($|A| > 2\nu_I$, $\nu_I$; the Larmor frequency of nucleus) hyperfine couplings. ED-NMR spectra of (d) sample D and (f) samples F with much superior S/N ratio, which is measured for only a few hours, exhibit a big advantage in the detection of hyperfine couplings. Some bumps, that are ascribed to strong hyperfine couplings, are observed at around ± 40 MHz in (d) and ± 30–40 (in a good agreement with the ENDOR spectra), 80–100, and 150–165 MHz in (f).

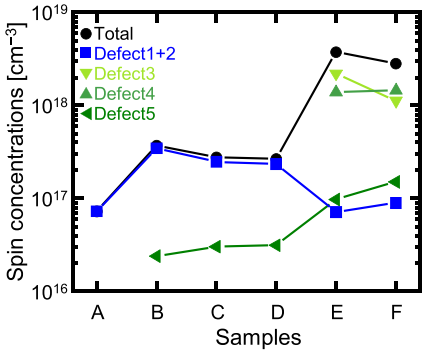


**Fig. 6.** Spin concentration of samples A-F. Total concentrations are obtained by comparisons with reference samples (TEMPO solutions). The concentration of each defect is obtained by simulations (see SI for the detailed evaluation procedures). We were unable to distinguish defect 1 from defect 2 in Barium rich condition. We arbitrarily attributed their combined intensities to defect 1.

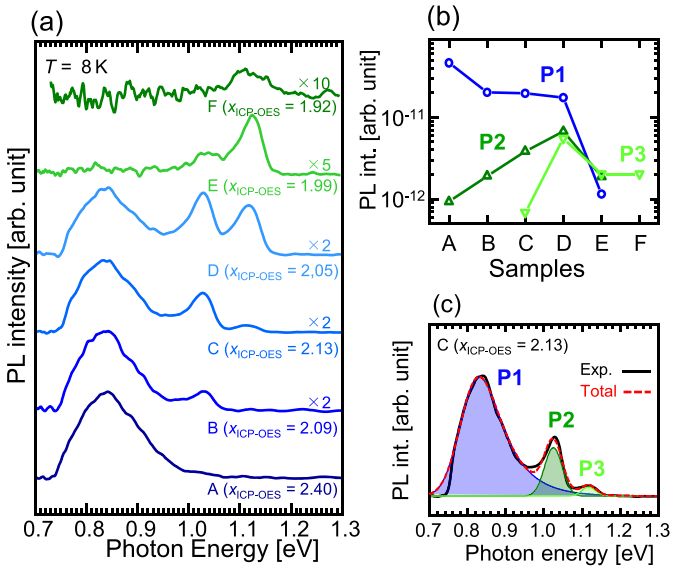


**Fig. 7.** (a) Photoluminescence (PL) spectra of Samples A-F measured at 8 K. The relative intensity of each peak is plotted in (b). The observed PL spectra can be decomposed of three PL bands (c).

intensities which vary with atomic composition. In a previous study, we reported similar variations for $BaSi_2$ epitaxial films and polycrystalline $BaSi_2$ samples.[33] We emphasize here that the predominant PL peak in Si-rich samples (P1) was drastically decreased in Ba-rich samples (Fig. 7b).

We investigated the temperature and excitation-intensity dependences of the PL spectra (Figs. S17-19 ). As the temperature increased, the PL peaks were quenched at different rates. Increasing temperature caused the peak positions of P1 and P2 to shift toward higher photon energies (blueshift), whereas P3 underwent a redshift (Figure S19(a)). These observations, and the fact that the shape of the emission bands varies with excitation power, indicate that the emitting

species are of different natures. The variation of the integrated intensities $I_{PL}$ of the PL bands with the excitation power $L$ follows a superlinear power law of the type $I_{PL} \propto L^{\kappa}$, where the values of $\kappa$ correspond to various transition mechanisms (Figure S18). As outlined by Spindler *et al.*,[57] these $\kappa$ values provide information on the nature of the transitions: donor-to-acceptor ($\kappa < 1$), deep-donor-to-acceptor ($\kappa < 1$), or free-to-band ($\kappa > 1$). All the PL bands in our samples had $\kappa$ values of less than 1, inferring that they are associated with defects. The features of the PL bands derived from the excitation intensity-dependent PL spectra are summarized in Table 3.

These PL active defects form energy levels of varying depth in the gap, which localize the charges that interact with the vibrations of the surrounding lattice, the so-called electron-phonon interaction (EPI). If we consider low amplitudes of chemical bond vibrations, we can represent their effect on the energy of the emitting state and the ground state as two harmonic oscillators (see Fig. 11). The abscissa of the harmonic oscillators (the configuration coordinate) represent the amplitude of vibration of a given vibrational mode, generally a breathing mode. EPI results in a shift of the emitting state along the configuration coordinate with respect to the ground state, and the greater the EPI coupling, the greater this shift. The consequence is that EPI produces a gap $E_{dis} = E_{ab}$ - $E_{PL}$ between the energy $E_{ab}$ of the absorption peak and the energy $E_{PL}$ of the emission peak (the Stoke shift) (Fig. 11), and increases the width $w$ of the absorption and emission bands. The importance of EPI is quantified by the Huang-Rhys parameter $S$ linked to the Stoke shift $E_{dis}$ by $E_{dis} = S.E_{ph}$, where $E_{ph}$ is the phonon energy.[58] The line shape is highly dependent on EPI strength. For a nearly zero EPI (corresponding to $S = 0$), the absorption and PL lines are very thin and overlap zero-phonon line, ZPL. For $S \geq 1$, the emission maximum appears at an energy $(S\text{-}1/2)E_{ph}$ lower than the ZPL, and its line shape becomes dissymmetrical (Pekarian shape) and tends towards Gaussian for large EPI, i.e. $S \approx 10$. The expression of the lineshape as a function of $S$ and $E_{ph}$ is quite complex,[58] and we cannot measure $S$ from $E_{dis}$ without identifying the corresponding absorption band, which makes it impossible to reproduce the PL lineshape. Instead, we simulated the PL bands by a mathematical expression for a dissymmetric Gaussian, as successfully used for Ge,[59,60] (Fig. 7(c))

$$\mathrm{I(E)} = \frac{\mathrm{A}}{\mu}\exp\left[\frac{1}{2}\left(\frac{\omega}{\mu}\right)^2 - \frac{\mathrm{E} - \mathrm{E_{PL}}}{\mu}\right]\int_{-\infty}^{z}\frac{1}{\sqrt{2\pi}}\exp\left(-\frac{z^2}{2}\right)dz,$$

where $A$, $\omega$, $E$, and $E_{PL}$ are the amplitude of the PL band, the width of the Gaussian component, the photon energy, and the position of the PL peak, respectively. The distortion of the Gaussian is represented by a skewness factor $\mu$, included in the variable $z$ as follows:

$$z = \frac{\mathrm{E} - \mathrm{E_{PL}}}{\omega} - \frac{\omega}{\mu}$$

**Table 3**
Nature of the observed PL bands. Each band peaks at a distinct peak position as seen in Fig. 7(c). PL intensity, $I_{PL}$, increases superlinearly with an increase of excitation power, $L$, ($I_{PL} \propto L^{\kappa}$, $\kappa < 1$), indicating that the band would be ascribed to the transitions associated with the defect-induced states in the gap. A shift of the peak position (peak shift), activation energy ($E_a$), Huang-Rhys factor ($S$), average phonon energy ($E_{ph}$), and skewness factor ($\mu$) are derived from temperature dependency of the PL bands. See the details in the text and SI.

| Label | P1 | P2 | P3 |
|---|---|---|---|
| Peak position [eV] | 0.84 | 1.05 | 1.14 |
| Exitation power dependency | | | |
| $\kappa$ | 0.53 | 0.55 | 0.70 |
| Temperature dependency | | | |
| Peak shift | Blue shift | Blue(?) shift | Red shift |
| $E_a$ [meV] | 16–18 | 5–38 | 10 |
| $S$ | 7 | 1 | – |
| $E_{ph}$ [meV] | 9 | 6 | – |
| $\mu$ | 0.06 | 0.005 | 0.003 |

The result of simulation for sample C is shown in Fig. 7(c).

The magnitude of the EPI can be roughly estimated from the temperature variation of the PL bandwidth $w(T)$:[61]

$$w(\mathrm{T}) = w(0)\left[coth\left(\frac{\langle E_{ph}\rangle}{2k_BT}\right)\right]^{\frac{1}{2}}$$

where $w(0) = 2.36\langle E_{ph}\rangle\sqrt{S}$ is the second moment of the Pekarian-shape bandwidth.[58] Here, $\langle E_{ph}\rangle$ is the average phonon energy during light emission. The width of P1 and P2 is temperature dependent, whereas the width of P3 is not (see Figure S19(c)). The above equation reproduces temperature dependencies with $S \approx 7$ and $\langle E_{ph}\rangle \approx 9$ meV for P1 and $S \approx 1$ and $\langle E_{ph}\rangle \approx 6$ meV for P2. Each $S$ value corresponds to a specific shape of PL band. This correspondence was systematically investigated by L. Pavesi and M. Guzzi.[62] According to their classification, the relatively large value of $S = 7$ infers a strong EPI.[61,63] The estimated average phonon energy ($\langle E_{ph}^{em}\rangle$) of 9 meV is in good agreement with the Raman spectroscopy phonon frequency (68 $cm^{-1}$ = 8.6 meV at RT).[64] Ab initio calculations of phonon DOSs revealed that phonon frequencies in the range of 50–98 $cm^{-1}$ (6–12 meV) were composed of motions of Ba ions.[65] Thus, P1 could plausibly be associated with a defect that both induces the deep defect level and strongly interacts with the lattice vibrations.

The temperature quenching of the PL is due to the presence of thermally accessible (activation energy $E_a$) competing level for a non-radiative pathway, which controls the temperature-dependency of the PL intensity:[66]

$$I(T) = \frac{I_0}{1 + \phi_1 T^{3/2} + \phi_2 T^{3/2}\exp(-E_a/k_BT)}.$$

Here, $I_0$, $\phi_1$, and $\phi_2$ are constants, and $k_B$ is the Boltzmann constant. All the PL bands for our samples were thermally quenched above 100 K, and their activation energies were a few tens of meV (see SI, Figure S19 (b)). The small activation energies compared to the PL peak energies indicate that, in addition to deep defects, relatively shallow states near the VB or the CB contribute to the PL bands (see Fig. 11).

### 3.4. DFT computations

#### 3.4.1. Formation energies

*3.4.1.1. Intrinsic defects and oxygen defects.* The primary focus of our investigation was paramagnetic (EPR-active) defects, but diamagnetic (neutral and charged) defects were also considered. We started our DFT investigations by computing formation energies for the six intrinsic points defects $V_{Si}/Si_i$, $V_{Ba}/Ba_i$ and $Ba_{Si}/Si_{Ba}$ using the procedure developed by Kumar et al. for both Si-rich and Ba-rich conditions (Fig. 8 and SI: Figs. S26-S27; Tables S6–11).[35] We checked that we reproduced their results.

In Si-rich conditions, and with a Fermi energy expected in the middle of the band gap (Fig. 8, left), the most favorable defects were silicon vacancies $V_{Si}$ with charges +1, 0, −1, and neutral silicon interstitial $Si_i$ and antisite defect $Ba_{Si}$. In Ba-rich conditions (Fig. 8, center), $V_{Si}$ was in competition with $Ba_{Si}$, whereas $Si_i$ was pushed higher in the energy scale. All other defects had much higher formation energies and, most probably, are not present in high enough concentrations to produce detectable spectroscopic signals.

For (oxygen-based) extrinsic defects, we first considered interstitial oxygen $O_i$ (Fig. 8, right) in Si-rich conditions (also see SI: Figs. S28-S31; Tables S12–13). This defect had a negative formation energy, indicating that insertion of oxygen into $BaSi_2$ material is thermodynamically favorable, as reported in the literature.[67]

*3.4.1.2. Complex defects.* We also investigated more complex defects.

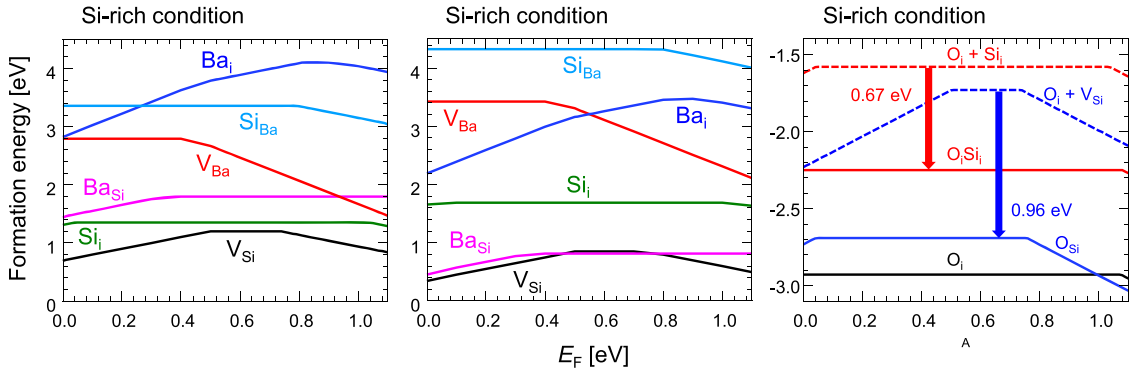


**Fig. 8.** Calculated formation energies as a function of the Fermi energy for intrinsic (neutral and charged) point defects in $BaSi_2$ under Si-rich (left) and Ba-rich (center) conditions (cf. Fig. 5 of Kumar et al., Mater. Chem. A, 2017, 5, 25,293). Calculated formation energies as a function of the Fermi energy for extrinsic (oxygen-based) point defects in $BaSi_2$ under Si-rich conditions (right). Comparison between complex [$O_{Si}$] (blue lines), isolated $O_i$ (black line) and complex [$O_iSi_i$] (red lines) defects. For both complex defects, we plot their respective gains relative to the energy sum of their isolated parents: $V_{Si}$ and $O_i$ (dotted blue line) for $O_{Si}$, and $Si_i$ and $O_i$ (dotted red line) for [$Si_iO_i$].

We first considered the pseudo-tetrahedron [$OSi_3$] noted $O_{Si}$ (Fig. 9(a)). This defect can be considered to result from the combination of $V_{Si}$ and $O_i$: $V_{Si} + O_i \rightarrow O_{Si}$. By DFT, we found $O_{Si}$ to be more stable than the sum of its isolated parent defects $V_{Si} + O_i$ by 0.96 eV in the (8c) site. In contrast with $O_i$, which was only found in its neutral diamagnetic state $O_i(q = 0)$ for all Fermi energy values, $O_{Si}$ (blue continuous line, Fig. 8 right) had charge transition levels from diamagnetic $q = 0$ (formal $O^{-1}$ atom) to paramagnetic $q{=}{-}1$ (formal $O^{-2}$ atom), separated by 0.76 eV. It should be noted that, according to our calculations, the formation energy for an $O_{Si}$ defect in a (4c) site is only 0.2 eV greater than the formation energy for the same defect in an (8c) site. All properties for this defect are reported in Table 2.

We also tested the possibility that intrinsic $Si_i$ defects were stabilized by the nearby presence of oxygen: $Si_i + O_i \rightarrow [Si_iO_i]$. For oxygen insertion, as the A site is 0.41 eV more stable than the C site, we constructed the complex [$Si_iO_i$] based on A insertion sites (SI: Figure S28). We tested two configurations for [$Si_iO_i$] complexes involving two filled A sites: one with Si and one with O. In the first model, both O and Si were inserted within nearby A sites along the b axis (see SI: Figure S30A) with an initial Si…O distance of 3.41 Å (final distance between the two atoms: 3.41 Å, though with a distorted local geometry). In the second model, O and Si involved A sites on adjacent Si-A-Si chains (see SI: Figure S30B) with a longer initial Si…O distance (7.92 Å; final distance: 4.80 Å, once again with distorted geometries) (Fig. 9(b)). The formation energy of the second complex [$Si_iO_i$] model was more stable by 0.52 eV (see details in SI), and its formation energy was 0.67 eV lower than the sum of the formation energies of its isolated parents. Due to the many possibilities of combining $Si_i$ and $O_i$ defects (including combinations of A and C sites), these results remain preliminary. We therefore cannot rule out the possibility that other configurations would have even lower formation energies. Nevertheless, our analysis serves to show that, in the presence of oxygen, $Si_i$ defects will most probably not be found alone in the bulk material, but will be stabilized by nearby $O_i$ defects through the formation of [$Si_iO_i$] complexes. Once all $Si_i$ have been paired with oxygen atoms, additional oxygen atoms will continue to fill other insertion sites (in which case, once again, A sites are the most stabilized. See SI, Figure S30C and Table S13).

### 3.4.2. *EPR spectroscopic parameters*

We computed EPR parameters (g tensor, hyperfine coupling tensor, and quadrupolar tensors) for the three most stable intrinsic point defects $V_{Si}$, $Si_i$ and $Ba_{Si}$ as well as for (isolated) $O_i$ and two oxygen-containing complexes [$O_{Si}$] and [$Si_iO_i$]: see Table 2.

We first noticed that some defect models ($O_i^{+1}$, $[O_iSi_i]^{-1}$) exhibit very

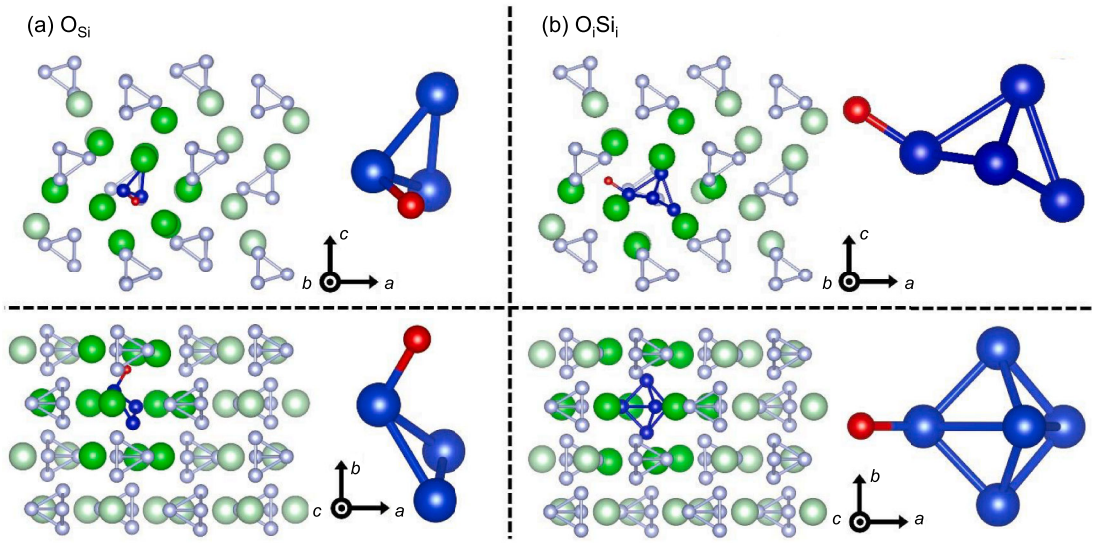


**Fig. 9.** General geometries for the complex defects containing oxygen investigated in this work (oxygen atoms in red, silicon atoms in blue, barium atoms in green). a) $O_{Si}$ defect in the neutral state b) $S_iO_i$ defect in the neutral state. For each defect, two orientation are given.

large anisotropies, as measured by the $\Delta g$ ($= g_3 - g_1$) parameter. Consequently, at least some splittings between filled and empty states are very small. These splittings contribute to these g tensors, and consequently the $g_i$ values computed are associated with greater uncertainty.

As for the computed hyperfine tensors, we found generally substantial $^{29}$Si hyperfine anisotropies (in the range [17-126] MHz), with two exceptions, both being paramagnetic $O_i$ defects. In contrast, $^{137}$Ba hyperfine anisotropies were all small (below 29 MHz).

Finally, we also computed $^{137}$Ba ($I = 3/2$) quadrupolar couplings (see SI: Table S20). All Ba quadrupolar coupling constants were in the range [38–49] MHz. All $\eta$ asymmetry parameters were smaller than 0.33, with the exception of −1 and +1 $Si_i$ defects ($\eta = 0.80$ and 0.86, respectively). These values are a signature of $Si_i$ defects impacting nearby $Ba^{2+}$ cations. The data pertaining to quadrupolar coupling were therefore not discriminating and have been omitted hereafter.

### 3.4.3. Photoluminescence (PL) results

From the formation energy diagrams presented in Fig. 8, we directly computed the corresponding charge transition levels (Fig. 10; Figure S37). In turn, these redox levels yielded the $E_{ZPL}$ values required to compute PL transitions (see below). Only $V_{Si}$, $Ba_{Si}$ and $O_{Si}$ exhibited charge transition levels well within the gap (deep levels). We can therefore anticipate that their PL lines will fall well below the DFT-computed gap value (1.1 eV; cf. Table S9). All other defects had charge transition levels close to either their valence-band maximum (VBM) or their conduction-band minimum (CBM). For these defects, PL lines close to the gap value are expected (see more below).

To compute PL lines, we considered two mechanisms (Fig. 11). In the D(rd/ox)e mechanism (Fig. 11 left), an electron is vertically excited into the CBM from a reduced defect level which becomes oxidized, first at constant geometry according to the Franck-Condon principle ($E_{ab}$ vertical absorption transition). The geometry of the oxidized defect then relaxes to equilibrium with a new configuration coordinate (reorganization energy, with a gain of $E_{ref}$). The excited electron reaches the CBM level and falls vertically to the level of the oxidized defect ($E_{PL}$ vertical emission); finally, this level relaxes back to its original reduced geometry ($E_{ref}$* energy gain).

A similar scenario applies to the D(ox/rd)h mechanism (Fig. 11 right). The electron is excited from the VBM into the oxidized defect level ($E_{ab}$* vertical absorption transition) which becomes reduced at constant geometry. The reduced defect then relaxes to equilibrium ($E_{ref}$* energy gain). PL occurs ($E_{PL}$* vertical emission), re-oxidizing the defect at constant geometry which relaxes back into its original ground state geometry ($E_{ref}$ energy gain).

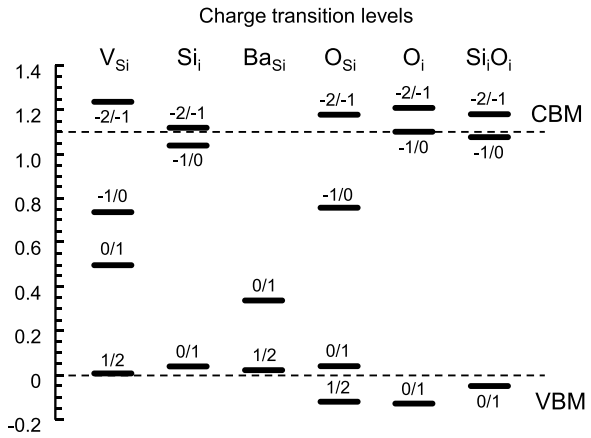


**Fig. 10.** Calculated charge transition levels for intrinsic ($V_{Si}$, $Si_i$ and $Ba_{Si}$) and extrinsic ($O_{Si}$ and $O_i$) defects. The charge changes are indicated for each level (cf. Figure S6 of Kumar et al.).

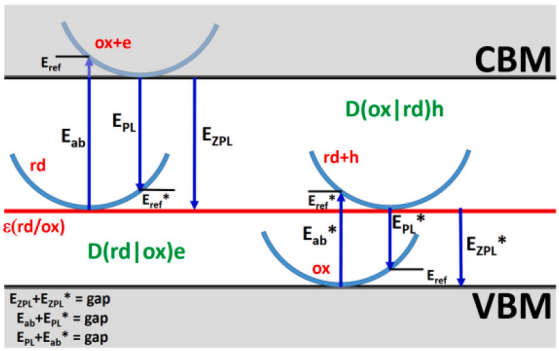


**Fig. 11.** Schematic representation of all energetic quantities needed to compute PL transitions for two mechanism: D(rd/ox)e (left) and D(ox/rd)h (right). In the D(rd/ox)e mechanism (left), an electron is vertically excited into the CBM from a reduced defect level which becomes oxidized, first at constant geometry according to the Franck-Condon principle ($E_{ab}$ vertical absorption transition). The geometry of the oxidized defect then relaxes to equilibrium with a new configuration coordinate (reorganization energy, with a gain of $E_{ref}$). The excited electron reaches the CBM level and falls vertically to the level of the oxidized defect ($E_{PL}$ vertical emission); finally, this level relaxes back to its original reduced geometry ($E_{ref}$* energy gain). In the D(ox/rd)h mechanism (right), the electron is excited from the VBM into the oxidized defect level ($E_{ab}$* vertical absorption transition) which becomes reduced at constant geometry. The reduced defect then relaxes to equilibrium ($E_{ref}$* energy gain). PL occurs ($E_{PL}$* vertical emission), re-oxidizing the defect at constant geometry which relaxes back into its original ground state geometry ($E_{ref}$ energy gain).

To compute PL transitions, it is not sufficient to calculate optimized oxidized and reduced geometries (i.e., charge transition levels) for a given defect (yielding $E_{ZPL}$ or $E_{ZPL}$*), we must also determine both $E_{ab}$ (absorption) and (PL) $E_{PL}$ terms. In addition, for a given geometry-optimized defect D of charge q (i.e., $D^q$), defects $D^{q-1}$ and $D^{q+1}$ must be computed at fixed $D^q$ geometry along with crossed terms, i.e., $D^q$ at fixed $D^{q-1}$ and $D^{q+1}$ geometries (see Tables S10–13). From these computations, we estimated all previously-mentioned transition terms relevant for PL (see Table 4 and Tables S14–15 for intrinsic defects, and Tables S16–17 for oxygen-based defects in Supporting Information).

All computed PL transitions between 0.6 eV and 1.1 eV are classified in decreasing order in Table 4. PL transitions corresponding to improbable (charge-wise) coulombic interactions such as D(+2|+1)h and D(-2|-1)e were then set aside (as indicated in the feasibility column in Table 4). The remaining PL values can be compared to the experimental PL lines: P0 (0.67 eV; Si-rich), P1 (0.84 eV; Si-rich), P2 (1.04 eV; Si-rich) and P3 (1.15 eV; Ba-rich). Here, P0 appears at the lower energy range with weaker intensity. Because our photomultiplier lacks the requisite sensitivity in the energy range to allow P0 to be recorded, we

**Table 4**
$E_{ab}$, $E_{ZPL}$ and $E_{PL}$ transitions computed for various transition types (cf. Fig. 10). By « feasible » is meant that the defect at the origin of the transition D(q| exists according to the formation energy diagrams (Fig. 8), allowing for $a \pm 0.1$ eV error window.

| type of transition | $E_{ab}$ (eV) | $E_{ZPL}$ (eV) | $E_{PL}$ (eV) | feasible |
|---|---|---|---|---|
| $O_{Si}(-1\|-2)h$ | *1.24* | *1.18* | *1.12* | no |
| $O_{Si}(+1\|+2)e$ | *1.47* | *1.22* | *1.10* | no |
| [OiSi](0\|+1)e | 1.37 | 1.25 | **1.08** | yes |
| [OiSi](0\|−1)h | 1.12 | 1.08 | **1.02** | yes |
| $Bas_i(+1\|+2)e$ | 1.13 | 1.08 | **1.03** | yes |
| $Vs_i(+1\|+2)e$ | 1.19 | 1.09 | **0.98** | yes |
| $Si_i(0\|+1)e$ | 1.18 | 1.06 | **0.95** | yes |
| $Si_i(-1\|-2)h$ | *1.26* | *1.12* | *0.93* | no |
| $O_{Si}(0\|+1)e$ | 1.21 | 1.06 | **0.77** | yes |
| $Si_i(0\|-1)h$ | 1.07 | 1.04 | **0.70** | yes |
| $Vs_i(-1\|0)e$ | 0.83 | 0.74 | **0.65** | yes |
| $O_{Si}(0\|-1)h$ | 0.86 | 0.76 | **0.65** | yes |
| $Bas_i(0\|+1)e$ | 0.80 | 0.76 | **0.62** | yes |

were unable to observe P0 in this study. However, given that Kishino et al.[17] found that P0 exists in Si-rich samples, it is plausible that our Si-rich samples also contain P0. Good DFT candidates were identified for each experimental PL line: 3 or 4 for P0 alone (last four lines of Table 4). P1 was broad (mid-height values around 0.77 and 0.90 eV) and could well correspond to $O_{Si}(0|+1)e$ (and possibly $Si_i(0|+1)e$, taking into account $a \pm 0.1$ eV DFT uncertainty). There were also four possible candidates for P2 and P3 (the first four feasible models in Table 4). The final choices are set out in the Discussion section, where we combined all experimental and theoretical inputs and constraints to yield a coherent picture of the material.

## 4. Discussion

### 4.1. Origin of defects

Structural characterization of all Si-rich and Ba-rich samples revealed that they are not homogeneous but biphasic. They all shared micrometer-size $BaSi_2$ stochiometric grains/domains. However, Si-rich samples also contained silicon inter-domains (Fig. 2a), in line with the fact that the pure silicon phase is next to $BaSi_2$ in the Ba-Si phase diagram, at high Si proportions (see SI: Section 4-1). Similarly, Ba-rich samples contained $Ba_3Si_4$ inter-domains (Fig. 2b), the phase next to $BaSi_2$ at high Ba proportions.[52]

This structural observation has major consequences when seeking to interpret EPR data. In effect, if the defects producing EPR signals 1–2 in Si-rich samples originated from silicon inter-domains, we would expect the intensities of the EPR lines to increase with increasing Si content (from D to A samples). However, this was not the case; Fig. 6 shows that the intensities of EPR signals 1–2 were nearly constant. The same reasoning applies to Ba-rich samples: larger excess of Ba (from E to F) structurally translates into more $Ba_3Si_4$ inter-domains, but the total intensity of EPR lines 3–5 was once again nearly constant. This experimental evidence from EPR signal intensities led us to hypothesize that *all* of the detected EPR signals derived from the common bulk-like $BaSi_2$ domains. Indeed, within Si-rich samples (A-D), the EPR signals were nearly identical from one sample to the next (Fig. 3). Ba-rich samples (E-F) showed a similar homogeneity, although the EPR signals recorded differed sharply from those obtained with Si-rich samples. Moreover, the total intensity of EPR signals made a significant quantitative jump (~10-fold increase) from Si-rich to Ba-rich domains (Fig. 6).

### 4.2. Intrinsic defects

If we consider only the most energetically favorable intrinsic defects, we could use a qualitative argument to simplify the attribution of EPR signals. Since the formation energies of defects in Ba-rich and Si-rich conditions are different, we should observe the same EPR-active species for Ba-rich and Si-rich samples, but with strong concentration changes (we assume that the Fermi energy level is roughly the same in the two conditions). In consequence, a simple comparison between panels of Fig. 8 indicates that EPR spectra for $Ba_{Si}^{+3}$/$Ba_{Si}^{+1}$/ $Ba_{Si}^{-1}$ and $V_{Si}^{+1}$/$V_{Si}^{-1}$ would be more intense in Ba-rich samples, and $Si_i^{+1}$/$Si_i^{-1}$ would be more intense in Si-rich samples. In all cases, if detectable in EPR, the $V_{Si}^{+1}$/$V_{Si}^{-1}$ would be the major species. In Ba-rich conditions the minor species would be $Ba_{Si}^{+3}$/$Ba_{Si}^{+1}$/ $Ba_{Si}^{-1}$, whereas in Si-rich conditions, $Si_i^{+1}$/ $Si_i^{-1}$ would be the minor species.

At this stage of the analysis, it is interesting to compare computed and experimental g tensor and hyperfine tensor values. In Ba-rich samples, we rapidly discarded defect 4 because of its overly-elusive nature (spin value, shape). As noted before, this elusiveness also creates considerable uncertainty as to its intensity. Defect 3 with a $\Delta g$ of 0.157 was also difficult to compare with DFT computations. It is important to point out that g tensor computations are particularly demanding for samples where anisotropies are large (i.e., small energy splitting). In our computations, no g tensor with this anisotropy could be found for the most stable intrinsic defects. One defect with a sizable g anisotropy was $Si_i^{+1}$ (only 0.066), but the g average was clearly above $g_e$, and the intensity of this species would increase drastically in Si-rich samples. This theoretical increase contrasts starkly with the experimental data. Since paramagnetic species with only a handful of well-separated states around the highest occupied state produce g tensors with a very small anisotropy, defect 3 is most probably the result of a shallow delocalized defect. Its very fast relaxation also suggests a species with excited states just above the fundamental state, again indicating a shallow defect. In addition, it was impossible to experimentally detect the hyperfine values for defects 3 and 4. Therefore, for the moment, the nature of defects 3 and 4 remains undetermined, but we are confident that these signals are not the result of localized deep point defects.

Defect 5, in contrast, was well characterized and good agreement was found between its experimental EPR parameters and the values computed for $V_{Si}^{-1}$ ($g_{av}$ around $g_e$, very small g anisotropy, several Ba hyperfine couplings between 80 MHz and 130 MHz, see Table 2). Since defect 5 is not the most intense species in the various Ba-rich conditions, we cannot formally discard the possibility that this defect corresponds to $Ba_{Si}^{3+}$ which is energetically very close to $V_{Si}^{-1}$. However, we can state that the concentration of either of them would be extremely low (Fig. 8) that is in the range $10^{15}$–$10^{16}$ per $cm^3$, as already found by Kumar *et al.* (cf. Eq. 4 and Fig.5d of therein).[35] We arrive at the same values using our own computed formation energy values, which are very similar to those published by Kumar et al (SI: Figure S38).

In Si-rich samples, we computed EPR parameters corresponding to experimental observations (defects 1–2, $g_{av}$ slightly above $g_e$). Although the g tensor for $Si_i^{+1}$/ $Si_i^{-1}$ fit rather well with defect 1 or defect 2 ($g_{av}$ above $g_e$), the anisotropy was too large. To interpret defect 1 and defect 2, we next examined intrinsic defects with higher formation energies. For instance, initially $Ba_{Si}^{+1}$ appears to be a good candidate with a sizable hyperfine coupling and a g tensor with moderate anisotropy and $g_{av}$ (2.020), above $g_e$. However, the concentration of this defect would be excessively low, contrasting starkly with the experimental results: in Si-rich samples, defect 1 and defect 2 are the major EPR species. In all cases, the concentrations of these defects must be very low compared with those of $V_{Si}^{+1}$/$V_{Si}^{-1}$, even in Si-rich conditions. We therefore cannot propose an obvious intrinsic candidate for defects 1 and 2.

### 4.3. Extrinsic complex defects

Another possibility is that something significant happens in Si-rich samples (by comparison with Ba-rich samples) to allow for the formation of new (i.e., non-intrinsic) defects. The key may lie in comparing the relative chemical affinities of $BaSi_2$, Si, or $Ba_3Si_4$ toward the first extrinsic element that comes to mind: oxygen. From basic chemistry principles and data (electronegativity of elements and formation enthalpy), we can infer that molecular oxygen will spontaneously react with these three compounds. Experimentally, $Ba_3Si_4$ is known to react faster with air (oxygen) and humidity than $BaSi_2$.[68] In other words, in Ba-rich samples, $Ba_3Si_4$ inter-domains are richer in electrons than $BaSi_2$, and can thus reduce and trap oxygen atoms. Conversely, Si-rich samples are electron-poor. Consequently, c-Si inter-domains are less prone to reduce oxygen than (more electron-rich) bulk-like $BaSi_2$ domains. We therefore expect oxygen to be preferentially present in $BaSi_2$ domains in Si-rich samples, where it would constitute a natural impurity/dopant. The results of element mapping (Fig. 2) support our analysis. In the Ba-rich sample, oxygen atoms tend to aggregate at the inter-domains, where $Ba_3Si_4$ precipitates. In Si-rich samples, oxygen atoms appear to be distributed over the entire sample. The striking difference between Ba-rich and Si-rich samples could therefore be due (at least in part) to the presence of specific oxygen-related defects in Si-rich samples, whereas in Ba-rich samples the intrinsic $V_{Si}^{-1}$ defect remains our best proposal.

In a previous study combining experimental and theoretical approaches, we had already observed sizable O atom concentrations in

$BaSi_2$ thin films, and noted an enhanced photoresponse.[69] In accordance with this work and previous ones, DFT calculations indicated that interstitial oxygen $O_i^0$ is indeed energetically favorable, with a negative formation energy of −2.93 eV.[67] However, in our super-cell [$Ba_{32}Si_{64}O$] comprising four individual cells (2 × 2 × 1 super-cell: see DFT Experimental Section), we found the most energetically favorable site to be site B (crystallographic 4a) (Fig. 1). Previous studies with a smaller (1 × 1 × 1) cell indicated that site C (crystallographic 4c) was favored.[69] We also tested whether complex defects involving $O_i$ paired with an intrinsic defect would show enhanced stabilization compared to isolated $O_i$. The most favorable configuration for $O_i + V_{Si} \rightarrow O_{Si}$ (notation aligned with that used for Ba antisite defects in $Ba_{Si}$) led to 0.96 eV greater stabilization compared to isolated $O_i$ and $V_{Si}$ (Fig. 8). In this case, the oxygen lies on the fourth corner of the tetrahedron and formally replaces the missing silicon atom (Fig. 9). For $O_i + Si_i$, in the most favorable configuration (0.67-eV greater stabilization), we found that the two defects did not spatially interact, being separated by 4.80 Å. We named this complex defect [$O_iSi_i$]. To the best of our knowledge, this is the first report of the existence of these complex defects.

Due to their extra stabilization energy, we can assume that in Si-rich conditions and in all four of our samples, nearly all $Si_i$ and $V_{Si}$ "react" first with oxygen before being transformed into [$Si_iO_i$] and $O_{Si}$ defects, respectively. The concentrations of [$Si_iO_i$] and $O_{Si}$ would thus be limited by those of the intrinsic parental defects ($Si_i$ and $V_{Si}$, respectively). This contrasts with the $O_i$ concentration, which will continue to increase when the sample is exposed to oxygen. As each oxygen atom has eight electrons, the most stable paramagnetic states of these three oxygen-containing defects will be $[Si_iO_i]^{+1/-1}$, $O_i^{+1}/O_i^{-1}$, and $O_{Si}^{+1/-1}$. We note that the formation energies for $O_{Si}^{+1}$, $O_i^{+1}$ and $[Si_iO_i]^{+1/-1}$ are 0.7 eV higher compared to $O_{Si}^{-1}$ (cf. Figs. S29 and S31). This corresponds to a factor of $\sim 10^{-5}$ in concentration. Because of their low concentrations, these defects would be undetectable by EPR. For $O_i^{-1}$, its formation energy is ~ 0.2 eV higher than that of $O_{Si}^{-1}$. Note that the actual concentration of $O_i$ is unknown because it will react to form $O_iSi_i$ (from $Si_i$) and $O_{Si}$ (from $V_{Si}$) complexes. Thus, $O_{Si}^{-1}$ is the most energetically favored complex defect. As shown in Table 2, the computed and experimental EPR parameters of $O_{Si}^{-1}$ defects agreed well for Si-rich samples, with $g_{av}$ values slightly exceeding $g_e$, and hyperfine Barium couplings at 178 and 132 MHz for the Si5 site (8c). Another crystallographic position was found (Si4, 4c) for $O_{Si}$, for which the formation energy was just 0.2 eV greater. Its g tensor and hyperfine values were even more compatible with the experimental EPR parameters determined for defect 1 and defect 2. We can thus attribute these two EPR paramagnetic species – which have very similar properties (g tensor, intensity, relaxation time, etc.) – to the same type of defect, $O_{Si}^{-1}$, but with a slightly different environment. As mentioned above, the exhaustive exploration and computation of all complex defects would be very difficult and time-consuming due to the number of degrees of freedom involved. However, we are confident that the two optimized geometries identified are representative of complex oxygen-containing defects.

From the point of view of the optical properties of the defects, we can now finalize our defect assignments. Given the affinity of Si-rich samples for oxygen, the dominant PL bands, P0 and P1, can be ascribed to $O_{Si}(0|-1)$h and $O_{Si}(0|+1)$e, respectively (Table 4). As expected, these PL bands disappeared in Ba-rich samples. This dramatic transition complies with our hypothesis: as oxygen is trapped by $Ba_3Si_4$ in Ba-rich samples, intrinsic defects become the main components in these systems. Since the absolute intensities of P2 and P3 tend to decrease in Ba-rich conditions, these PL transitions could also be produced by oxygen-related defects (most probably [$O_iSi_i$]). For instance, not only do the PL intensities of P2 and P3 follow a superlinear power law with $k < 1$, the activation energies of P2 and P3 also have a value of a few tens of meV, suggesting the existence of counterpart defects.

DLTS is often used to determine the electric nature of defects. In undoped $BaSi_2$ thin films, we found reports of five electrically-active defects.[29,30] Among them, the one positioned at approximately 0.2 eV below the CBM is reported in several publications, and roughly corresponds to the charge transition level for $O_{Si}^{(0|+1)}$ (0.34 eV below the CBM). However, DLTS analysis depends strongly on the temperature-dependence of carrier capture coefficients, trap levels, and on the bandgap. These parameters can cause significant estimation errors in the position of the trap level, we therefore leave our discussion of defect assignment here.[70]

In our previous study, we observed some EPR signals in a $BaSi_2$ thin-film with a well-controlled Si-to-Ba atomic ratio produced by tuning the experimental conditions during MBE growth.[71] The signals from this previous study are compatible with those observed in the (bulk) Si-rich systems used here (defect 1 and/or defect2). In particular, they exhibited g values above $g_e$ with a moderate g anisotropy (between 2.004 and 2.011), which is very close to the values of defect 1 or defect 2. In terms of photoresponsivity, optimal growth occurred under Si-rich conditions as close to stoichiometry as possible.[31] The low S/N ratio of the EPR signals obtained precluded a complete analysis, but we attributed them once again to $O_{Si}^{-1}$. As the $BaSi_2$ thin-film contains defect 1 and/or defect 2, its spin concentration was determined to be $5 \times 10^{14}$ $cm^{-3}$. Up to now, we have speculated that the carrier concentration in undoped $BaSi_2$ derives from defects that were unintentionally incorporated into the system, such as Si vacancies. Interestingly, the spin concentration determined by DFT roughly corresponds to the carrier concentration of $\sim 10^{15}$ $cm^{-3}$ determined elsewhere.[72]

### 4.4. Implications for doping and passivation

Observation of these complex oxygen-based defects by EPR in bulk as well as $BaSi_2$ thin films is very interesting, and may help to better understand previous observations, such as the behavior observed by Du et al., whereby oxygen "doping" increased the photoresponsivity of a $BaSi_2$ thin-film.[69] One explanation for this enhanced responsivity could be that oxygen neutralizes active defects located deep within the structure. We therefore examined our DFT computations to determine whether [$O_iSi_i$] or $O_{Si}$ could be considered neutralized versions of the intrinsic $Si_i$ and $V_{Si}$ defects. The energy variations between $V_{Si}^{(0|+1)}$ and $O_{Si}^{(0|+1)}$ at charge transition level data (Fig. 10) were moderate, whereas the PL transitions were considerably altered. In particular, the deep-level PL transition $Si_i(0|-1)$h (see Table 4) at 0.70 eV was replaced by the equivalent [$O_iSi_i$](0|−1)h at 1.02 eV. This shift in PL values is mainly due to the very high reorganization energy computed for the $Si_i$ defect (0.3 eV) (see SI, Table S15).

Another important issue for photovoltaic applications is the need to be able to passivate defects with a view to substantially increasing the photoresponse of $BaS_2$ thin films. Our previous studies revealed that films post-treated by exposure to atomic hydrogen had a five-fold higher photoresponsivity than pristine films. Xu et al.[28] argued that electrical deactivation of the defect states induced by $V_{Si}$ could be achieved by three hydrogen atoms connected to a triangular [$Si_3$] cluster, improving photoresponsivity. However, our previous results indicate that the intrinsic defects $V_{Si}$ and $Si_i$ can be "consumed" in samples exposed to oxygen, leading to the formation of complex defects. These complex defects are particularly prevalent under the Si-rich conditions used during thin-film growth. It is thus important to analyze how hydrogenation affects these oxygen-based complex defects. Our computations show that one hydrogen atom preferentially interacts with an $O_{Si}$ defect rather than with a pristine silicon tetrahedron. The $O_{Si}H$ site was 1.25 eV more stable (SI: Section 4-6). Even more interestingly, a second hydrogen atom could also preferentially react with this mono-hydrogenated $O_{Si}H$ defect. The resulting $O_{Si}H_2$ site was 1.02 eV more stable. Based on these observations, we conclude that $O_{Si}$ defects are readily transformed into $O_{Si}H_2$ defects upon post-treatment with hydrogen.

For passivation to be efficient, it must remove as many deep levels as possible from within the band gap. We thus computed the spin-polarized

total DOS and atomically projected DOS's of $O_{Si}$, $O_{Si}H$, and $O_{Si}H_2$. $O_{Si}$ induces a defect state within the gap (Fig. 12), the components of which mainly originate from Si orbitals. At least some of these levels remained within the gap for $O_{Si}H$, indicating that addition of one hydrogen is not sufficient to produce complete passivation. It is striking that the addition of a second hydrogen (to form $O_{Si}H_2$) removed all defect levels from within the bandgap, effectively passivating these defects. We can interpret this hydrogen passivation effect by analogy with Si dangling-bond passivation by hydrogen in pure Si.[73] Such hydrogen passivation also applies in $BaSi_2$: as can be seen in Fig. 12, the atomically projected DOS for both Si and H are at the same energy level, indicating bonding/antibonding states resulting from overlapping orbitals belonging to both atoms.

These results contrast with the passivation process of $V_{Si}$ defects previously studied by Xu and al.,[28] who described hydrogen atoms also reacting readily with $V_{Si}$ defects. However, observation of the DOS reveals that some defect bands remain within the gap upon addition of two hydrogen atoms. A third hydrogen is therefore required to remove remaining states in the band gap, but causes the $BaSi_2$ to become a degenerate semiconductor with an electron in the band gap. We can thus conclude that passivation is incomplete. We consider that the experimental results showing a very significant photoresponse increase upon passivation with H atoms can be better explained with $O_{Si}$ defects than with $V_{Si}$ defects.

## 5. Conclusions

This is the first systematic study of the defects in $BaSi_2$ grown in a range of conditions combining experimental measurements - EPR, PL - with DFT computation. Our results showed that in Ba-rich conditions, the EPR signals most probably originate from intrinsic defects, with defect 5 corresponding to $V_{Si}^{-1}$. In Si-rich conditions, oxygen plays a crucial role by interacting with intrinsic defects to form complex defects. EPR observations indicate that defect 1 and defect 2 correspond to the negatively charged complex defect $O_{Si}^{-1}$, consisting of a pseudotetrahedron of 3 silicon atoms and 1 oxygen atom. For PL, we attributed band P0 and band P1 to transitions involving this $O_{Si}^{-1}$ defect, whereas P2 and P3 involved $[O_iSi]$, another complex defect consisting of an interstitial silicon interacting with an interstitial oxygen. The DFT calculations showed that presence of these complex defects can explain some properties of $BaSi_2$ thin films, in particular their efficient passivation by hydrogen atoms. The results presented here will pave the way toward a better understanding and control of the defects in $BaSi_2$.

## CRediT authorship contribution statement

**Takuma Sato:** Writing – review & editing, Writing – original draft, Visualization, Validation, Investigation, Formal analysis, Data curation. **Jean-Marie Mouesca:** Writing – review & editing, Writing – original draft, Visualization, Validation, Investigation, Formal analysis, Data curation, Conceptualization. **Anne-Laure Barra:** Resources, Investigation, Data curation. **Didier Gourier:** Writing – review & editing,

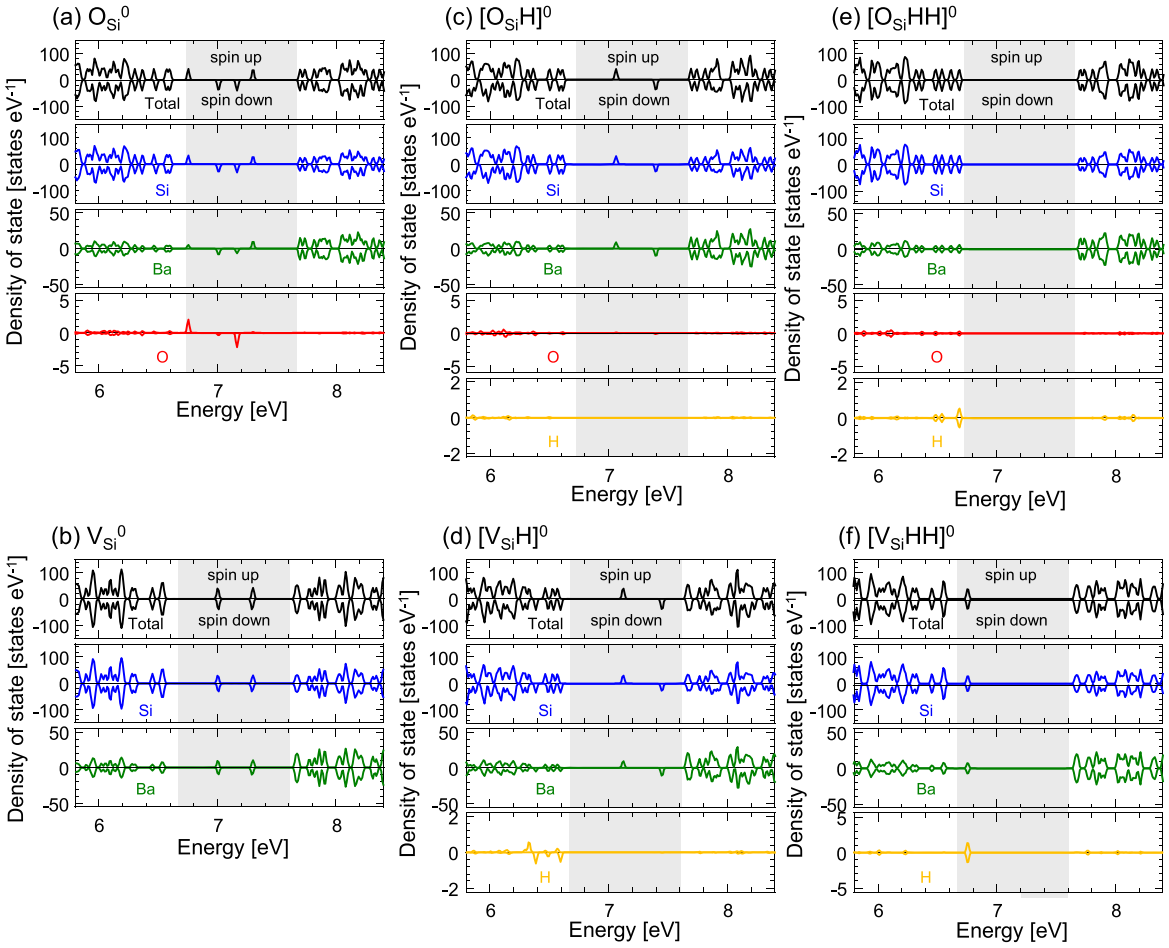


**Fig. 12.** Spin-polarized density of states (DOS) of (a) $O_{Si}$, (b) $O_{Si}H$, (c) $O_{Si}HH$, (d) $V_{Si}$, (e)$V_{Si}H$, and (f) $V_{Si}HH$. The charge state of the models is neutral. Atomically projected spin-polarized DOSs of the models show how individual atoms contribute to the formation of the defect-induced state within the gap. The band gap is hatched by grey-colored areas.

Validation, Formal analysis. **Motoharu Imai:** Writing – review & editing, Validation, Resources, Investigation, Data curation. **Takashi Suemasu:** Writing – review & editing, Supervision, Resources, Project administration, Conceptualization. **Serge Gambarelli:** Writing – review & editing, Writing – original draft, Validation, Supervision, Resources, Project administration, Methodology, Investigation, Funding acquisition, Formal analysis, Data curation, Conceptualization.

## Declaration of interests

The authors declare that they have no known competing financial interests or personal relationships that could have appeared to influence the work reported in this paper.

## Acknowledgments

J.-M. M. thanks the HPC/AI resources of TGCC for the allocation of computing resource (2022- AD010913560) by GENCI (DFT/QE calculations). J.M. M. and S. G. thank T. Deutsch (CEA/DRF/IRIG/DEPHY/MEM) and Joël Eymery (CEA/DRF/IRIG/DEPHY/MEM/NRX) for helpful discussions. We especially acknowledge the help of Damien Caliste (CEA/DRF/IRIG/DEPHY/MEM/L_SIM) in understanding the energetics of charged models. M.I. thanks M. Nishio of the National Institute for Materials Science (NIMS) for EPMA, K. Yamada and A. Ishitoya of NIMS for the ICP-OES. M.I. acknowledges financial support from JSPS KAKENHI (No. JP16K06713 and JP22H00268). T.S. acknowledges financial support from JSPS KAKENHI (No. JP17K18865 and JP18H03767).

## Supplementary materials

Supplementary material associated with this article can be found, in the online version, at doi:10.1016/j.actamat.2024.120230.

## References

[1] M. Imai, K. Hirata, T. Hirano, Superconductivity of trigonal $BaSi_2$, Phys. C Supercond. 245 (1995) 12–14, https://doi.org/10.1016/0921-4534(95)00082-8.
[2] J.A. Flores-Livas, R. Debord, S. Botti, A. San Miguel, M.A.L. Marques, S. Pailhès, Enhancing the Superconducting Transition Temperature of $BaSi_2$ by Structural Tuning, Phys. Rev. Lett. 106 (2011) 087002, https://doi.org/10.1103/PhysRevLett.106.087002.
[3] J.A. Flores-Livas, A. Sanna, Superconductivity in intercalated group-IV honeycomb structures, Phys. Rev. B 91 (2015) 054508, https://doi.org/10.1103/PhysRevB.91.054508.
[4] K. Hashimoto, K. Kurosaki, Y. Imamura, H. Muta, S. Yamanaka, Thermoelectric properties of $BaSi_2$, $SrSi_2$, and LaSi, J. Appl. Phys. 102 (2007) 063703, https://doi.org/10.1063/1.2778747.
[5] H. Peng, C. Wang, J. Li, R. Zhang, M.X. Wang, H. Wang, Y. Sun, M. Sheng, Lattice dynamic properties of $BaSi_2$ and $BaGe_2$ from first principle calculations, Phys. Lett. A 374 (2010) 3797–3800, https://doi.org/10.1016/j.physleta.2010.07.037.
[6] T. Ishibe, J. Chikada, T. Terada, Y. Komatsubara, R. Kitaura, S. Yachi, Y. Yamashita, T. Sato, T. Suemasu, Y. Nakamura, Low thermal conductivity of complex thermoelectric barium silicide film epitaxially grown on Si, Appl. Phys. Lett. 119 (2021) 141603, https://doi.org/10.1063/5.0063531.
[7] T. Suemasu, N. Usami, Exploring the potential of semiconducting $BaSi_2$ for thin-film solar cell applications, J. Phys. Appl. Phys. 50 (2016) 023001, https://doi.org/10.1088/1361-6463/50/2/023001.
[8] T. Suemasu, D.B. Migas, Recent Progress Toward Realization of High-Efficiency $BaSi_2$ Solar Cells: thin-Film Deposition Techniques and Passivation of Defects, Phys. Status Solidi A 219 (2022) 2100593, https://doi.org/10.1002/pssa.202100593.
[9] H. Schäfer, B. Eisenmann, W. Müller, Zintl-Phasen: übergangsformen zwischen Metall- und Ionenbindung, Angew. Chem. 85 (1973) 742–760, https://doi.org/10.1002/ange.19730851704.
[10] S.M. Kauzlarich, Chemistry, Structure, and Bonding of Zintl Phases and Ions: Selected Topics and Recent Advances, Wiley, 1996.
[11] W.B. Jensen, Abegg, Lewis, Langmuir, and the octet rule, J. Chem. Educ. 61 (1984) 191, https://doi.org/10.1021/ed061p191.
[12] T. Goebel, A. Ormeci, O. Pecher, F. Haarmann, The Silicides $M_4Si_4$ with M = Na, K, Rb, Cs, and $Ba_2Si_4$ – NMR Spectroscopy and Quantum Mechanical Calculations, Z. Für Anorg. Allg. Chem. 638 (2012) 1437–1445, https://doi.org/10.1002/zaac.201200198.
[13] M. Kumar, N. Umezawa, M. Imai, $BaSi_2$ as a promising low-cost, earth-abundant material with large optical activity for thin-film solar cells: a hybrid density functional study, Appl. Phys. Express 7 (2014) 071203, https://doi.org/10.7567/APEX.7.071203.
[14] M. Imai, M. Kumar, N. Umezawa, Electronic states of Zintl-phase solar-cell material $BaSi_2$, Scr. Mater. 172 (2019) 43–46, https://doi.org/10.1016/j.scriptamat.2019.07.004.
[15] M. Kumar, N. Umezawa, M. Imai, Recent advances in computational studies of thin-film solar cell material $BaSi_2$, Jpn. J. Appl. Phys. 59 (2020) SF0803, https://doi.org/10.35848/1347-4065/ab6b82.
[16] T. Nakamura, T. Suemasu, K. Takakura, F. Hasegawa, A. Wakahara, M. Imai, Investigation of the energy band structure of orthorhombic $BaSi_2$ by optical and electrical measurements and theoretical calculations, Appl. Phys. Lett. 81 (2002) 1032–1034, https://doi.org/10.1063/1.1498865.
[17] S. Kishino, T. Imai, T. Iida, Y. Nakaishi, M. Shinada, Y. Takanashi, N. Hamada, Electronic and optical properties of bulk crystals of semiconducting orthorhombic $BaSi_2$ prepared by the vertical Bridgman method, J. Alloys Compd. 428 (2007) 22–27, https://doi.org/10.1016/j.jallcom.2006.03.074.
[18] K. Toh, T. Saito, T. Suemasu, Optical Absorption Properties of $BaSi_2$ Epitaxial Films Grown on a Transparent Silicon-on-Insulator Substrate Using Molecular Beam Epitaxy, Jpn. J. Appl. Phys. 50 (2011) 068001, https://doi.org/10.1143/JJAP.50.068001.
[19] M. Baba, K. Toh, K. Toko, N. Saito, N. Yoshizawa, K. Jiptner, T. Sekiguchi, K. O. Hara, N. Usami, T. Suemasu, Investigation of grain boundaries in $BaSi_2$ epitaxial films on Si(1 1 1) substrates using transmission electron microscopy and electron-beam-induced current technique, J. Cryst. Growth 348 (2012) 75–79, https://doi.org/10.1016/j.jcrysgro.2012.03.044.
[20] K.O. Hara, N. Usami, K. Nakamura, R. Takabe, M. Baba, K. Toko, T. Suemasu, Determination of Bulk Minority-Carrier Lifetime in $BaSi_2$ Earth-Abundant Absorber Films by Utilizing a Drastic Enhancement of Carrier Lifetime by Post-Growth Annealing, Appl. Phys. Express 6 (2013) 112302, https://doi.org/10.7567/APEX.6.112302.
[21] K. Morita, Y. Inomata, T. Suemasu, Optical and electrical properties of semiconducting $BaSi_2$ thin films on Si substrates grown by molecular beam epitaxy, Thin Solid Films 508 (2006) 363–366, https://doi.org/10.1016/j.tsf.2005.07.344.
[22] M. Imai, M. Kumar, Y. Matsushita, N. Umezawa, Crystal structure and electronic properties of Sr-substituted barium disilicide $Ba_{1-x}Sr_xSi_2$ for solar cells: computational and experimental studies, Acta Mater 148 (2018) 492–498, https://doi.org/10.1016/j.actamat.2018.02.010.
[23] K.O. Hara, Y. Nakagawa, T. Suemasu, N. Usami, Realization of single-phase $BaSi_2$ films by vacuum evaporation with suitable optical properties and carrier lifetime for solar cell applications, Jpn. J. Appl. Phys. 54 (2015) 07JE02, https://doi.org/10.7567/JJAP.54.07JE02.
[24] M. Fujiwara, K. Takahashi, Y. Nakagawa, K. Gotoh, T. Itoh, Y. Kurokawa, N. Usami, Improved conversion efficiency of p-type $BaSi_2$/n-type crystalline Si heterojunction solar cells by a low growth rate deposition of $BaSi_2$, AIP Adv 12 (2022) 045115, https://doi.org/10.1063/5.0083812.
[25] K. Kodama, Y. Yamashita, K. Toko, T. Suemasu, Operation of $BaSi_2$ homojunction solar cells on $p^+$-Si(111) substrates and the effect of structure parameters on their performance, Appl. Phys. Express 12 (2019) 041005, https://doi.org/10.7567/1882-0786/ab0c4f.
[26] T. Suemasu, Exploring the possibility of semiconducting $BaSi_2$ for thin-film solar cell applications, Jpn. J. Appl. Phys. 54 (2015) 07JA01, https://doi.org/10.7567/JJAP.54.07JA01.
[27] Y. Yamashita, C.M. Ruiz Tobon, R. Santbergen, M. Zeman, O. Isabella, T. Suemasu, Solar cells based on $n^+$-AZO/p-$BaSi_2$ heterojunction: advanced opto-electrical modelling and experimental demonstration, Sol. Energy Mater. Sol. Cells 230 (2021) 111181, https://doi.org/10.1016/j.solmat.2021.111181.
[28] Z. Xu, D.A. Shohonov, A.B. Filonov, K. Gotoh, T. Deng, S. Honda, K. Toko, N. Usami, D.B. Migas, V.E. Borisenko, T. Suemasu, Marked enhancement of the photoresponsivity and minority-carrier lifetime of $BaSi_2$ passivated with atomic hydrogen, Phys. Rev. Mater. 3 (2019) 065403, https://doi.org/10.1103/PhysRevMaterials.3.065403.
[29] Y. Yamashita, T. Sato, M.E. Bayu, K. Toko, T. Suemasu, Investigation of electrically active defects in undoped $BaSi_2$ light absorber layers using deep-level transient spectroscopy, Jpn. J. Appl. Phys. 57 (2018) 075801, https://doi.org/10.7567/JJAP.57.075801.
[30] Y. Yamashita, T. Sato, N. Saitoh, N. Yoshizawa, K. Toko, T. Suemasu, Three-step growth of highly photoresponsive $BaSi_2$ light absorbing layers with uniform Ba to Si atomic ratios, J. Appl. Phys. 126 (2019) 215301, https://doi.org/10.1063/1.5128690.
[31] Y. Yamashita, Y. Takahara, T. Sato, K. Toko, A. Uedono, T. Suemasu, Simple way of finding Ba to Si deposition rate ratios for high photoresponsivity in $BaSi_2$ films by Raman spectroscopy, Appl. Phys. Express 12 (2019) 055506, https://doi.org/10.7567/1882-0786/ab14b9.
[32] A. Montes, S.W.H. Eijt, Y. Tian, R. Gram, H. Schut, T. Suemasu, N. Usami, M. Zeman, J. Serra, O. Isabella, Point defects in $BaSi_2$ thin films for photovoltaic applications studied by positron annihilation spectroscopy, J. Appl. Phys. 127 (2020) 085304, https://doi.org/10.1063/1.5126264.
[33] T. Sato, Y. Yamashita, Z. Xu, K. Toko, S. Gambarelli, M. Imai, T. Suemasu, Correlation of native defects between epitaxial films and polycrystalline $BaSi_2$ bulks based on photoluminescence spectra, Appl. Phys. Express 12 (2019) 111001, https://doi.org/10.7567/1882-0786/ab476f.
[34] M. Imai, T. Hirano, Electrical resistivity of metastable phases of $BaSi_2$ synthesized under high pressure and high temperature, J. Alloys Compd. 224 (1995) 111–116, https://doi.org/10.1016/0925-8388(95)01530-2.

[35] M. Kumar, N. Umezawa, W. Zhou, M. Imai, Barium disilicide as a promising thin-film photovoltaic absorber: structural, electronic, and defect properties, J. Mater. Chem. A 5 (2017) 25293–25302, https://doi.org/10.1039/C7TA08312B.

[36] Y. Nishi, Study of Silicon-Silicon Dioxide Structure by Electron Spin Resonance I, Jpn. J. Appl. Phys. 10 (1971) 52, https://doi.org/10.1143/JJAP.10.52.

[37] B.P. Lemke, D. Haneman, Dangling bonds on silicon, Phys. Rev. B 17 (1978) 1893–1907, https://doi.org/10.1103/PhysRevB.17.1893.

[38] K.L. Brower, $^{29}$Si hyperfine structure of unpaired spins at the Si/$SiO_2$ interface, Appl. Phys. Lett. 43 (1983) 1111–1113, https://doi.org/10.1063/1.94244.

[39] P.M. Lenahan, J.F. Conley, What can electron paramagnetic resonance tell us about the Si/$SiO_2$ system? J. Vac. Sci. Technol. B Microelectron. Nanometer Struct. Process. Meas. Phenom. 16 (1998) 2134–2153, https://doi.org/10.1116/1.590301.

[40] T. Umeda, M. Nishizawa, T. Yasuda, J. Isoya, S. Yamasaki, K. Tanaka, Electron Spin Resonance Observation of the Si(111)-(7×7) Surface and Its Oxidation Process, Phys. Rev. Lett. 86 (2001) 1054–1057, https://doi.org/10.1103/PhysRevLett.86.1054.

[41] P. Höfer, A. Grupp, H. Nebenführ, M. Mehring, Hyperfine sublevel correlation (hyscore) spectroscopy: a 2D ESR investigation of the squaric acid radical, Chem. Phys. Lett. 132 (1986) 279–282, https://doi.org/10.1016/0009-2614(86)80124-5.

[42] E.R. Davies, A new pulse endor technique, Phys. Lett. A 47 (1974) 1–2, https://doi.org/10.1016/0375-9601(74)90078-4.

[43] P. Schosseler, Th. Wacker, A. Schweiger, Pulsed ELDOR detected NMR, Chem. Phys. Lett. 224 (1994) 319–324, https://doi.org/10.1016/0009-2614(94)00548-6.

[44] T. Suemasu, K.O. Hara, H. Udono, M. Imai, Silicon meets group-II metals in energy and electronic applications—How to handle reactive sources for high-quality films and bulk crystals, J. Appl. Phys. 131 (2022) 191101, https://doi.org/10.1063/5.0092080.

[45] T. Hetzke, A.M. Bowen, T.F. Prisner, ELDOR-detected NMR at Q-Band, Appl. Magn. Reson. 48 (2017) 1375–1397, https://doi.org/10.1007/s00723-017-0927-4.

[46] S. Stoll, A. Schweiger, EasySpin, a comprehensive software package for spectral simulation and analysis in EPR, J. Magn. Reson. 178 (2006) 42–55, https://doi.org/10.1016/j.jmr.2005.08.013.

[47] P. Giannozzi, S. Baroni, N. Bonini, M. Calandra, R. Car, C. Cavazzoni, D. Ceresoli, G.L. Chiarotti, M. Cococcioni, I. Dabo, A.D. Corso, S. de Gironcoli, S. Fabris, G. Fratesi, R. Gebauer, U. Gerstmann, C. Gougoussis, A. Kokalj, M. Lazzeri, L. Martin-Samos, N. Marzari, F. Mauri, R. Mazzarello, S. Paolini, A. Pasquarello, L. Paulatto, C. Sbraccia, S. Scandolo, G. Sclauzero, A.P. Seitsonen, A. Smogunov, P. Umari, R.M. Wentzcovitch, QUANTUM ESPRESSO: a modular and open-source software project for quantum simulations of materials, J. Phys. Condens. Matter 21 (2009) 395502, https://doi.org/10.1088/0953-8984/21/39/395502.

[48] J.P. Perdew, K. Burke, M. Ernzerhof, Generalized Gradient Approximation Made Simple, Phys. Rev. Lett. 77 (1996) 3865–3868, https://doi.org/10.1103/PhysRevLett.77.3865.

[49] P. Giannozzi, O. Andreussi, T. Brumme, O. Bunau, M.B. Nardelli, M. Calandra, R. Car, C. Cavazzoni, D. Ceresoli, M. Cococcioni, N. Colonna, I. Carnimeo, A. D. Corso, S. de Gironcoli, P. Delugas, R.A. DiStasio, A. Ferretti, A. Floris, G. Fratesi, G. Fugallo, R. Gebauer, U. Gerstmann, F. Giustino, T. Gorni, J. Jia, M. Kawamura, H.-Y. Ko, A. Kokalj, E. Küçükbenli, M. Lazzeri, M. Marsili, N. Marzari, F. Mauri, N. L. Nguyen, H.-V. Nguyen, A. Otero-de-la-Roza, L. Paulatto, S. Poncé, D. Rocca, R. Sabatini, B. Santra, M. Schlipf, A.P. Seitsonen, A. Smogunov, I. Timrov, T. Thonhauser, P. Umari, N. Vast, X. Wu, S. Baroni, Advanced capabilities for materials modelling with Quantum ESPRESSO, J. Phys. Condens. Matter 29 (2017) 465901, https://doi.org/10.1088/1361-648X/aa8f79.

[50] J. Evers, G. Oehlinger, A. Weiss, A New High-Pressure Phase of Barium Disilicide, Angew. Chem. Int. Ed. Engl. 17 (1978) 538–539, https://doi.org/10.1002/anie.197805381.

[51] T. Goebel, Y. Prots, F. Haarmann, Refinement of the crystal structure of dibarium tetrasilicide, $Ba_2Si_4$, Z. Für Krist. New Cryst. Struct. 224 (2009) 7–8, https://doi.org/10.1524/ncrs.2009.0005.

[52] M. Pani, A. Palenzona, The phase diagram of the Ba–Si system, J. Alloys Compd. 454 (2008) L1–L2, https://doi.org/10.1016/j.jallcom.2006.12.065.

[53] D.S. Marlin, E. Bill, T. Weyhermüller, E. Bothe, K. Wieghardt, Magnetic Interactions in Dinuclear $Mn^{III}Mn^{IV}$ Complexes Covalently Tethered to Organic Radicals: Spectroscopic Models for the $S_2Y_Z^{\bullet}$ State of Photosystem II, J. Am. Chem. Soc. 127 (2005) 6095–6108, https://doi.org/10.1021/ja042655w.

[54] H. Quast, W. Nüdling, G. Klemm, A. Kirschfeld, P. Neuhaus, W. Sander, D. A. Hrovat, W.T. Borden, A Perimidine-Derived Non-Kekulé Triplet Diradical, J. Org. Chem. 73 (2008) 4956–4961, https://doi.org/10.1021/jo800589y.

[55] D. Goldfarb, S. Stoll, E.P.R. Spectroscopy, Fundamentals and Methods, John Wiley & Sons, 2018.

[56] N. Wili, A primer in pulse EPR-based hyperfine spectroscopy for NMR spectroscopists, J. Magn. Reson. Open 16–17 (2023) 100108, https://doi.org/10.1016/j.jmro.2023.100108.

[57] C. Spindler, T. Galvani, L. Wirtz, G. Rey, S. Siebentritt, Excitation-intensity dependence of shallow and deep-level photoluminescence transitions in semiconductors, J. Appl. Phys. 126 (2019) 175703, https://doi.org/10.1063/1.5095235.

[58] B. Henderson, G.F. Imbusch, B. Henderson, G.F. Imbusch, Optical Spectroscopy of Inorganic Solids, Oxford University Press, Oxford, New York, 1989, pp. 197–209.

[59] Eli. Grushka, Characterization of exponentially modified Gaussian peaks in chromatography, Anal. Chem. 44 (1972) 1733–1738, https://doi.org/10.1021/ac60319a011.

[60] F. Pezzoli, L. Qing, A. Giorgioni, G. Isella, E. Grilli, M. Guzzi, H. Dery, Spin and energy relaxation in germanium studied by spin-polarized direct-gap photoluminescence, Phys. Rev. B 88 (2013) 045204, https://doi.org/10.1103/PhysRevB.88.045204.

[61] Y. Toyozawa, Further Contribution to the Theory of the Line-Shape of the Exciton Absorption Band, Prog. Theor. Phys. 27 (1962) 89–104, https://doi.org/10.1143/PTP.27.89.

[62] L. Pavesi, M. Guzzi, Photoluminescence of $Al_xGa_{1-x}As$ alloys, J. Appl. Phys. 75 (1994) 4779–4842, https://doi.org/10.1063/1.355769.

[63] W. Stadler, D.M. Hofmann, H.C. Alt, T. Muschik, B.K. Meyer, E. Weigel, G. Müller-Vogt, M. Salk, E. Rupp, K.W. Benz, Optical investigations of defects in $Cd_{1-x}Zn_xTe$, Phys. Rev. B 51 (1995) 10619–10630, https://doi.org/10.1103/PhysRevB.51.10619.

[64] M. Somer, Vibrational Spectra of the Cluster Anions $[E_4]^{4-}$ in the metallic Sodium and Barium Compounds $Na_4E_4$ and $Ba_2E_4$ (E = Si, Ge), Z. Für Anorg. Allg. Chem. 626 (2000) 2478–2480, https://doi.org/10.1002/1521-3749(200012)626:12<2478::AID-ZAAC2478>3.0.CO;2-A.

[65] M. Ramesh, M.K. Niranjan, Phonon modes, dielectric properties, infrared reflectivity, and Raman intensity spectra of semiconducting silicide $BaSi_2$: first principles study, J. Phys. Chem. Solids 121 (2018) 219–227, https://doi.org/10.1016/j.jpcs.2018.05.033.

[66] J. Krustok, J. Raudoja, M. Yakushev, R.D. Pilkington, H. Collan, Photoluminescence study of deep levels in $CuGaTe_2$ crystals, J. Appl. Phys. 86 (1999) 5305–5307, https://doi.org/10.1063/1.371517.

[67] Y. Imai, M. Sohma, T. Suemasu, Energetic evaluation of possible interstitial compound formation of BaSi $_2$ with 2p-, 3s-, and 3d-elements using first-principle calculations, Jpn. J. Appl. Phys. 54 (2015) 07JE03, https://doi.org/10.7567/JJAP.54.07JE03.

[68] B. Eisenmann, K.H. Janzon, H. Schäfer, A. Weiss, Notizen: zur Kenntnis von $Ba_3Si_4$, Z. Für Naturforschung B 24 (1969) 457–458, https://doi.org/10.1515/znb-1969-0421.

[69] W. Du, R. Takabe, S. Yachi, K. Toko, T. Suemasu, Enhanced spectral response of semiconducting $BaSi_2$ films by oxygen incorporation, Thin Solid Films 629 (2017) 17–21, https://doi.org/10.1016/j.tsf.2017.03.046.

[70] D. Wickramaratne, C.E. Dreyer, B. Monserrat, J.-X. Shen, J.L. Lyons, A. Alkauskas, C.G. Van de Walle, Defect identification based on first-principles calculations for deep level transient spectroscopy, Appl. Phys. Lett. 113 (2018) 192106, https://doi.org/10.1063/1.5047808.

[71] T. Sato, C. Lombard, Y. Yamashita, Z. Xu, L. Benincasa, K. Toko, S. Gambarelli, T. Suemasu, Investigation of native defects in $BaSi_2$ epitaxial films by electron paramagnetic resonance, Appl. Phys. Express 12 (2019) 061005, https://doi.org/10.7567/1882-0786/ab2062.

[72] R. Takabe, T. Deng, K. Kodama, Y. Yamashita, T. Sato, K. Toko, T. Suemasu, Impact of Ba to Si deposition rate ratios during molecular beam epitaxy on carrier concentration and spectral response of $BaSi_2$ epitaxial films, J. Appl. Phys. 123 (2018) 045703, https://doi.org/10.1063/1.4994850.

[73] A.H. Edwards, Interaction of H and $H_2$ with the silicon dangling orbital at the <111>Si/$SiO_2$ interface, Phys. Rev. B 44 (1991) 1832–1838, https://doi.org/10.1103/PhysRevB.44.1832.